RESEARCH ARTICLE | MARCH 05 2025

Laminar-turbulent transition in a hypersonic compression ramp flow

Changye Huang (黄长烨) ; Shibin Cao (曹石彬) ; Jiaao Hao (郝佳傲) ; Peixu Guo (郭培旭) ;
Chih-Yung Wen (温志湧)

Physics of Fluids 37, 034110 (2025)
https://doi.org/10.1063/5.0256584

Physics of Fluids
AIP Publishing

Physics of Fluids ARTICLE pubs.aip.org/aip/pof

Laminar-turbulent transition in a hypersonic compression ramp flow

Cite as: Phys. Fluids **37**, 034110 (2025); doi: 10.1063/5.0256584
Submitted: 6 January 2025 · Accepted: 12 February 2025 ·
Published Online: 5 March 2025

View Online Export Citation CrossMark

Changye Huang (黄长烨),[a] Shibin Cao (曹石彬),[b] Jiaao Hao (郝佳傲), Peixu Guo (郭培旭),
and Chih-Yung Wen (温志湧)

AFFILIATIONS

Department of Aeronautical and Aviation Engineering, The Hong Kong Polytechnic University, Kowloon, Hong Kong, China

[a]Electronic mail: changye.huang@connect.polyu.hk
[b]Author to whom correspondence should be addressed: shibincao@outlook.com

ABSTRACT

The hypersonic flow over a compression ramp is investigated by utilizing direct numerical simulation (DNS) and various stability analysis tools. The free-stream Mach number and Reynolds number based on the length of the flat plate are 8.0 and 3.9×10^5, respectively. Global stability analysis is applied to confirm the weekly unstable nature of the current flow condition. As a result of the low growth rate, this case is believed to be more susceptible to convective instability than intrinsic instability. Subsequently, across a wide range of frequencies and a globally stable wavelength, resolvent analysis is utilized to investigate the response of two-dimensional base flow to external disturbances. It reveals that the optimal response to upstream disturbances located adjacent to the leading edge manifests in the form of streamwise streaks, which result from transient growth in the flat-plate boundary layer. Downstream of reattachment, the Mack second mode and low-frequency streaks as a manifestation of Görtler instability coexist within the boundary layers. Further downstream, the amalgamation of the amplification of Mack's second mode with the sinuous and varicose breakdown of streaks disrupts the boundary layers via the ejection-sweep motion, resulting in the creation of a strong localized vorticity region and contributing to the concentration of vorticity within the boundary layers. This kicks off the vortex roll-up process, which results in the formation of hairpin vortices, and eventually leads to the breakdown process.

I. INTRODUCTION

The interaction between the shock wave and laminar boundary layer is a prevalent issue in fluid mechanics and has a significant practical impact on the aerodynamics and propulsion of high-speed flight vehicles.[1,2] Compression ramp flow, shock impingement on a flat plate, and double-cone flow are typical configurations exemplifying the interaction between shock waves and laminar boundary layers.[3,4] When the pressure rise induced by the shock wave reaches a sufficient magnitude, the boundary layer becomes incapable of resisting the adverse pressure gradient and consequently separates from the wall, resulting in the formation of a separation bubble.[5] The separated flow induced by shock waves can accommodate numerous local and global instabilities, which may result in unsteadiness and eventually the laminar-turbulent transition.[6–8] Laminar-turbulent transition within the boundary layers of a hypersonic vehicle has the potential to significantly enhance surface heating rates and increase frictional drag, and it is a fundamental subject in the design of hypersonic vehicles.[9,10] Therefore, comprehending and anticipating boundary-layer transitions is of great significance in hypersonic flight.

There exist various pathways leading to turbulence within flat plate boundary layers, including eigenmode growth, transient growth, and bypass mechanisms, depending on the amplitude of environmental disturbances.[11] Due to the complexity of flow structures, such as flow separation, the stability and transition mechanisms of flows involving the shock wave and boundary layer interaction can be significantly different from flat plate boundary layer flows. For instance, in the case of hypersonic shock wave and boundary layer interaction flows that are accompanied by strong flow separation and dominated by intrinsic instability, the intrinsic instability can lead to the occurrence of transition scenarios.[12,13] It is noteworthy that irrespective of whether the shock wave and boundary layer interaction flow is intrinsically unstable or stable, convective instabilities can play a significant role in destabilizing the flow, as external disturbances are typically prominent during high-speed flights. As a result, transition paths that apply to boundary layers may persist in shock wave and boundary layer interactions.[13] For example, Lugrin *et al.*[14] investigated a transitional flow passing through a hollow cylinder/flare numerically and identified several potential transition paths, such as the Mack second mode, oblique mode, etc. Not coincidentally, for a compression ramp at Mach 5.373 at an angle of 5.5°, a three-dimensional wave packet triggered by a wall-blowing suction pulse upstream of separation was conducted by Novikov *et al.*[15] They demonstrated that the evolution of the wave packet is dominated by either the planar second mode or the oblique first mode, contingent upon the precise location of the pulse. As described by Hao *et al.*[16] in hypersonic compression flow, streamwise streaks could be energetic enough to trigger secondary instabilities and the subsequent breakdown into turbulence, and in the scenario where streamwise streaks survive the breakdown process and are dissipated by viscosity as transported downstream, the second mode evolving in the reattached boundary layer can trigger transitions through nonlinear resonance.[17]

Due to additional complexities, such as the coexistence of the Mack second mode instability,[18,19] crossflow instability,[20] Görtler instability,[21,22] and nonlinear coupling of different processes, the hypersonic laminar-turbulent transition is less understood compared with incompressible flows.[23,24] It is widely acknowledged that the Mack second mode exhibits the fastest-growing instability in high-speed boundary layers under certain configurations, such as flat plates and slender geometries at zero angle of attack, typically exceeding Mach 4.[25,26] In contrast to the conventional first-mode instability, the second mode, longitudinal acoustic waves reflected between the relative sonic line and the solid wall, is gaining great significance at high Mach numbers.[27] Balakumar *et al.*[28] utilized linear stability analysis along with DNS to determine the behavior of two-dimensional, fixed-frequency perturbations within a flat plate boundary layer as it encounters a 5.5° compression ramp at Mach 5.4. Their results indicated that the secondary mode waves exhibit neutral stability while traversing the separated shear layer, yet exhibit an exponential growth upstream of separation and downstream of reattachment. Novikov *et al.*[15] performed DNS of 3-D broad-spectrum wave packets using the same configuration. Wave packets dominated by oblique and second-mode waves were examined. It was found that in the upstream portion of the separation bubble, the latter were neutrally stable before amplifying downstream. Their results indicated that the wave packet tail was stretched by the strong force, and turbulent spots were formed downstream of reattachment. Butler and Laurence[29] conducted experimental investigations concerning the evolution of second-mode waves within an incipiently separated compression-corner shock wave and boundary layer interaction. They observed that at high Reynolds numbers, the corner interaction leads to a rapid breakdown immediately after reattachment, resulting in a faster transition than for a straight cone. Subsequently, they carried out experimental research to investigate the transition from laminar to turbulent flow that occurs when there is a sharp increase in the surface angle on a slender body at Mach 6.[30] Their findings indicated that in the scenario with a 5° compression, the flow field is dominated by the Mack second mode disturbances, which tend to transition into turbulence more rapidly when they encounter a change in angle. If not limited to shock wave and boundary layer interaction, in terms of flat plate boundary layer flows, Casper *et al.*[31] conducted experimental research on the nonlinear evolution of the second-mode instability within wave packets at Mach 6, ultimately leading to the formation of turbulent spots, by utilizing non-intrusive measurements. In addition, high-speed Schlieren techniques have made possible spectral, time-frequency and topology analyses of second-mode disturbances in hypersonic boundary layer flows.[32] Franko and Lele[33] focused on the transitional features triggered by second-mode instabilities through fundamental resonance and oblique mode breakdown, employing DNS. Not limited to that, the relative dominance of K-type resonance mechanisms in hypersonic cones over H-type resonance has been quantified by Sivasubramanian and Fasel[34,35] utilizing controlled excitation with wave packets and harmonic waves. The experiments mentioned above were mostly conducted in conventional-noise facilities to study the laminar-turbulent transition. These facilities experienced amplified disturbances not found in the flight environment. It is therefore difficult to achieve a laminar separation, especially at higher Reynolds numbers, which could bias the transition mechanism. Benitez *et al.*[36] conducted quiet-flow experimental tests on a cone-cylinder-flare configuration, which provided a free stream environment to mimic the flight and resulted in a laminar separation. They found that the Mack second mode was neutrally stable over the separation bubble. Meanwhile, their experiments showed the amplification of lower-frequency oblique waves, likely related to the Mack first mode.[37] They further demonstrated the nonlinear interaction of those convective instabilities with the Mack second mode ultimately resulting in the generation of turbulent spots downstream of reattachment.[38]

Another type of stability that has been extensively studied is known as Görtler instability, which is attributed to an imbalance between the centrifugal force and the wall-normal pressure gradient, resulting in the formation of spanwise-periodic and streamwise-elongated streaks.[39] In the case of the compression ramp configuration, the highly curved streamline formed around the reattachment point contributes to the emergence of Görtler instability,[40,41] and the streamwise streaks are generally referred to as the footprint of Görtler-like vortices. There just exists a limited number of experimental studies examining the Görtler instability with curved surfaces in high-speed flows. Huang *et al.*[42–44] performed a series of experimental works at Mach 6.5 and captured transition phenomena that developed naturally or were triggered by roughness. These preliminary phenomena serve to illustrate the onset of Görtler instability in hypersonic flows with curved geometry, encompassing the emergence of Görtler vortices and their secondary instability modes during transition processes. Görtler instability, in addition to the concave wall configuration, can also be detected in dual incident shock wave and turbulent boundary layer interaction experiments.[45] Numerical simulations have been employed by numerous researchers to uncover the underlying structures and the corresponding fundamental mechanisms of Görtler instability. For a curved wall with a flat plate configuration at Mach 6.5, Chen *et al.*[46,47] confirmed the existence of the Görtler and Mack modes and elucidated the breakdown process of the secondary Görtler instability through wall blowing and suction. Subsequently, this configuration has been adopted to assess the stabilizing impacts of grooves on Görtler instability and transition features triggered by low-frequency blowing and suction.[48,49]

Despite the substantial amount of research on hypersonic transitional boundary layer flows, elucidating the transition mechanisms responsible for the observed transition phenomena in shock wave and boundary layer interactions still poses challenges. For instance, the transition phenomena and potential transition mechanisms that result from the combined effects of Görtler instability and the Mack second mode in hypersonic compression flows. In the present study, we examine transition features resulting from the amalgamation of Görtler instability and the Mack second mode using a compression ramp configuration. To clarify the stability of the considered hypersonic compression flow, stability analysis tools, such as global stability analysis, resolvent analysis, and linear stability analysis, are employed. To further elucidate the transitional nature, we performed three-dimensional DNS and proposed possible transition mechanisms as a response to the white noise introduced upstream of the separation point and downstream of the leading-edge shock. The noise is in the form of a spanwise velocity perturbation with an amplitude of 0.06.

The remainder of this paper is organized as follows. Section II describes the geometric configuration, flow conditions, stability analysis tools, and DNS details. Section III presents the base flow features, and introduces the analysis results of global stability analysis, resolvent analysis, and DNS. A possible transition mechanism is proposed in Sec. IV. Section V gives concluding remarks.

II. COMPUTATIONAL DETAILS

A. Geometric configuration and flow conditions

The geometric configuration used in the numerical calculation is compression ramp geometry, which is composed of a flat plate with a sharp leading edge and a ramp with a deflection angle of 15°.[50] The lengths of the flat plate and the ramp utilized in the current numerical calculation are $L = 50$ mm and $L_r = 100$ mm, respectively. The flow conditions are from the experiment of Chuvakhov and Radchenko,[50] which are shown as follows: Free stream Mach number $M_\infty = 8.0$, incoming flow static temperature $T_\infty = 53.26\,\mathrm{K}$, Reynolds number $Re_L{=}3.9\times10^5$, static pressure $P_\infty = 353\,\mathrm{Pa}$ and density $\rho_\infty = 0.0231\mathrm{kg/m^3}$. The short run time of the shock tunnel permits the application of an isothermal wall boundary condition, with the corresponding wall temperature T_w of 293 K, corresponds to a wall-to-total temperature ratio of 0.399.

B. Direct numerical simulation

DNS using the finite-difference method with high-order accuracy in both space and time and with shock-capturing capability is employed to study the hypersonic compression-ramp flow problem, and this code has been successfully applied to study hypersonic compression-ramp flows.[13,40,51–53] The 3D Navier–Stokes equations are employed in a conservative form for current unsteady, compressible flows.

$$\frac{\partial \boldsymbol{U}}{\partial t}+\frac{\partial \boldsymbol{F}}{\partial x}+\frac{\partial \boldsymbol{G}}{\partial y}+\frac{\partial \boldsymbol{H}}{\partial z}=\frac{\partial \boldsymbol{F}^{v}}{\partial x}+\frac{\partial \boldsymbol{G}^{v}}{\partial y}+\frac{\partial \boldsymbol{H}^{v}}{\partial z}, \tag{1}$$

where $\boldsymbol{F}$, $\boldsymbol{G}$ and $\boldsymbol{H}$ denote inviscid fluxes, $\boldsymbol{F}^v$, $\boldsymbol{G}^v$ and $\boldsymbol{H}^v$ are viscous fluxes. $\boldsymbol{U} = (\rho, \rho u, \rho v, \rho w, \rho e)^{\mathrm{T}}$ is the conservative variables vector, ρ denotes the density, u, v, and w are flow velocities along x, y, and z directions, respectively. Another variable e denotes the total energy per unit mass, and T means the transpose of the matrix. The perfect gas law is adopted to close the equation system, with the specific gas constant $R = 287\mathrm{J/(kg\cdot K)}$. Sutherland's law is utilized to assess the dynamic viscosity. For the current simulation, the Prandtl number Pr and specific heat ratio γ are set to 0.72 and 1.4, respectively.

Regarding the numerical methods, time integration is executed through an explicit third-order total variation diminishing Runge–Kutta scheme.[54] A weighted essentially non-oscillatory (WENO) scheme of fifth order is utilized to discretize the inviscid fluxes, based on the work of Jiang and Shu.[55] A sixth-order central-difference scheme is utilized to approximate the viscous fluxes. Further information regarding the numerical schemes can be obtained from Hermes *et al.*,[56] Cao *et al.*,[52] and Cao.[57]

In the two-dimensional base flow simulation, the number of grid points along streamwise (x) and vertical (y) directions is 3612 and 220, respectively. As shown in Appendix A, this mesh configuration is sufficient to capture the two-dimensional flow features. For the three-dimensional case, 200 grid points are evenly spaced along the spanwise direction over a width of 16 mm, corresponding to a total number of grid points of $3612 \times 220 \times 200 = 159$ million. This mesh configuration yields the subsequent non-dimensional wall units located near the outflow region ($x/L = 2.93$): $x^+ = 5.5$, $y^+ = 0.8$, and $z^+ = 9.8$. Regarding the boundary conditions, free-stream parameters are specified at the inflow and upper boundaries. For the outflow boundary, the zero-gradient extrapolation condition is employed. For the no-slip wall, isothermal conditions are specified, and the wall temperature is specified to be 293 K. For the three-dimensional case, periodic boundary conditions are implemented along the spanwise direction.

C. Global stability analysis

An in-house global stability analysis solver is used to evaluate the temporal stability of a two-dimensional base flow subject to three-dimensional small-amplitude disturbances that are periodic in the spanwise direction.[13,40,51,58] The conservative variable vector, $\boldsymbol{U}$, is decomposed into a two-dimensional steady solution $\boldsymbol{U}_{2D}$ and a three-dimensional small-amplitude perturbation $\boldsymbol{U}'$ as follows:

$$\boldsymbol{U}(x,y,z,t)=\boldsymbol{U}_{2D}(x,y)+\boldsymbol{U}'(x,y,z,t). \tag{2}$$

Linearized Navier–Stokes (LNS) equations describing the behavior of $\boldsymbol{U}'$ can then be obtained.

$$\frac{\partial \boldsymbol{U}'}{\partial t}+\frac{\partial \boldsymbol{F}'}{\partial x}+\frac{\partial \boldsymbol{G}'}{\partial y}+\frac{\partial \boldsymbol{H}'}{\partial z}=\frac{\partial \boldsymbol{F}^{v'}}{\partial x}+\frac{\partial \boldsymbol{G}^{v'}}{\partial y}+\frac{\partial \boldsymbol{H}^{v'}}{\partial z}, \tag{3}$$

where the prime indicates the perturbation variables. The Navier–Stokes equations that have been linearized can additionally be expressed in operator form.

$$\frac{\partial \boldsymbol{U}'}{\partial t}=A\boldsymbol{U}', \tag{4}$$

where A denotes the LNS operator. It is further presumed that the perturbation $\boldsymbol{U}'$ exists in the modal form:

$$\boldsymbol{U}'(x,y,z,t)=\hat{\boldsymbol{U}}(x,y)\exp\left[\mathrm{i}\frac{2\pi}{\lambda}z-\mathrm{i}(\omega_r+\mathrm{i}\omega_i)t\right], \tag{5}$$

where $\hat{\boldsymbol{U}}$ indicates the two-dimensional eigenfunction, λ denotes the wavelength in the spanwise direction, ω_i is the growth rate, and the angular frequency is represented by ω_r. Here, $\omega_r = 2\pi f$, where f denotes the frequency. By substituting Eq. (5) into Eq. (4) and discretizing the result using the finite volume method, the eigenvalue problem is obtained

$$\boldsymbol{A}(\lambda)\hat{\boldsymbol{U}}=-\mathrm{i}(\omega_r+\mathrm{i}\omega_i)\hat{\boldsymbol{U}}, \tag{6}$$

where $\boldsymbol{A}(\lambda)$ represents the global Jacobian matrix. The solution to the eigenvalue problem is achieved through the implementation of the implicit restarted Arnoldi method in ARPACK.[59] A shift-invert method is utilized to explore the corresponding eigenvalue spectra effectively. For further information, please refer to Hao *et al.*[58]

Due to the lower-upper decomposition of the global matrix performed during the inversion step, the shift-invert method is extremely expensive in terms of computational memory. The mesh information for the base flow for the stability analysis is 1225 × 240 to minimize computational resources, and the corresponding geometric information is that the length of the flat plate and the ramp are both 50 mm. Grid independence verification was performed using another set of finer grids (1750 × 340). The grid independence verification results can be referred to in Appendix B.

D. Resolvent analysis

The response of two-dimensional globally stable base flow to external small-amplitude perturbations $\boldsymbol{f}'$ with temporal and spanwise periodicity is considered in the present resolvent analysis. The operator form for the corresponding LNS equations is provided below:

$$\frac{\partial \boldsymbol{U}'}{\partial t} = A\boldsymbol{U}' + B\boldsymbol{f}', \tag{7}$$

where operator B restricts the force to a localized location (i.e., $x/L = 0.2$), which is under subsequent three-dimensional DNS. The expression of $\boldsymbol{f}'$ is:

$$\boldsymbol{f}'(x, y, z, t) = \hat{\boldsymbol{f}}(x, y)\exp\left(\mathrm{i}\frac{2\pi}{\lambda}z - \mathrm{i}\omega_r t\right). \tag{8}$$

It is important to note that, as time progresses to infinity, all initial perturbations imposed on the globally stable base flow decay to zero. That is, the long-time solution of Eq. (8) has the same form as the forcing and is given by the following equation:

$$\boldsymbol{U}'(x, y, z, t) = \hat{\boldsymbol{U}}(x, y)\exp\left(\mathrm{i}\frac{2\pi}{\lambda}z - \mathrm{i}\omega_r t\right). \tag{9}$$

By substituting Eqs. (8) and (9) into Eq. (7) and discretizing the result in the same manner as in the global stability analysis, the following result is obtained:

$$\hat{\boldsymbol{U}} = \boldsymbol{R}B\hat{\boldsymbol{f}}, \tag{10}$$

$$\boldsymbol{R} = (-\mathrm{i}\omega_r\boldsymbol{I} - \boldsymbol{A})^{-1}, \tag{11}$$

where matrix $\boldsymbol{R}$ represents resolvent matrix, B indicates the aforementioned constraint matrix and $\boldsymbol{I}$ is the identity matrix.

The objective of the resolvent analysis is to identify the forcing and response pairs that optimize the energy amplification defined by:

$$\sigma^2(\lambda, \omega_r) = \max_{\hat{f}} \frac{\|\hat{\boldsymbol{U}}\|_E}{\|B\hat{\boldsymbol{f}}\|_E}, \tag{12}$$

where σ denotes the optimal gain, and the Chu energy is utilized to obtain the energy norm:

$$\|\hat{\boldsymbol{U}}\|_E = \hat{\boldsymbol{U}}^*\boldsymbol{M}\hat{\boldsymbol{U}} \tag{13}$$

where $\boldsymbol{M}$ denotes the weight matrix and $\hat{\boldsymbol{U}}^*$ is the complex conjugate of $\hat{\boldsymbol{U}}$. According to the research conducted by Sipp and Marquet,[60] Bugeat *et al.*,[61] and Dwivedi *et al.*,[62] the optimization problem in Eq. (12) can be transformed into an eigenvalue problem:

$$B^*\boldsymbol{M}^{-1}\boldsymbol{R}^*MRB\hat{\boldsymbol{f}} = \sigma^2\hat{\boldsymbol{f}}, \tag{14}$$

which can be resolved by utilizing ARPACK for the given β (β is the spanwise wavenumber, $\beta = \frac{2\pi}{\lambda}$) and ω_r in the regular mode. Super-LU is employed to calculate the inverses of $\boldsymbol{R}$ and its conjugate transpose during this procedure. The maximal eigenvalue signifies the optimal gain squared, whereas the corresponding eigenfunction denotes the optimal forcing.[16,40] Using Eqs. (10) and (11), the optimal response can be readily ascertained.

III. RESULTS AND ANALYSIS

A. Two-dimensional base flow

Figure 1 depicts a schematic representation of the base flow structure over the current compression corner configuration. Figures 1(a) and 1(b) provide the Mach number contour and enlargement view superimposed with streamlines within the separation bubble, respectively. As depicted in Fig. 1(a), the separation bubble emerges around the corner as a result of the pressure rise induced by the ramp shock, with the separation and reattachment points located at $x/L = 0.48$ and 1.44, respectively. As shown in Fig. 1(b), there is no secondary separation formed under this incoming flow condition.

Figures 2(a) and 2(b) show the comparison of numerical schlieren and experimental schlieren visualization results from Chuvakhov and Radchenko.[50] As a result of the viscous interaction, a weak leading edge shock is generated. The adverse pressure gradient caused by the flow deflection causes a separation region near the corner, which further induces a separation shock and a reattachment shock. The slip line and expansion wave are formed by the interaction between separation and reattachment shock waves. It is apparent from Figs. 2(a) and 2(b) that the locations of separation points and reattachment points obtained by DNS are in good agreement with the experimental results, i.e., the size of the separation bubble matches well with each other. Figure 2(c) presents the comparison results between the experiment[50] and DNS in terms of the Stanton number (St) distribution along the

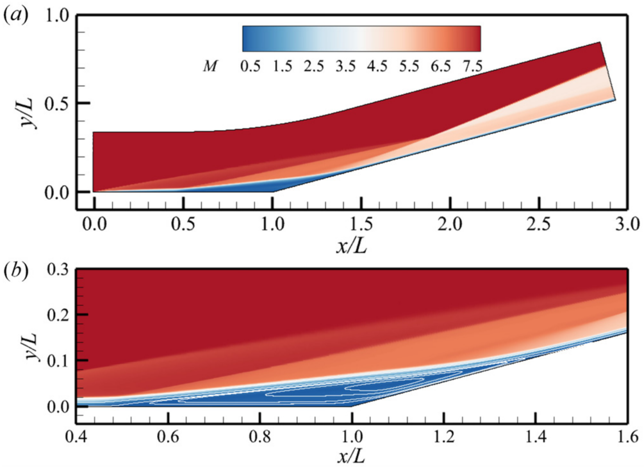

FIG. 1. Visualization of base flow: (a) Mach number contour and (b) Enlarged view of Fig. 1(a) superimposed with streamlines within the separation bubble.

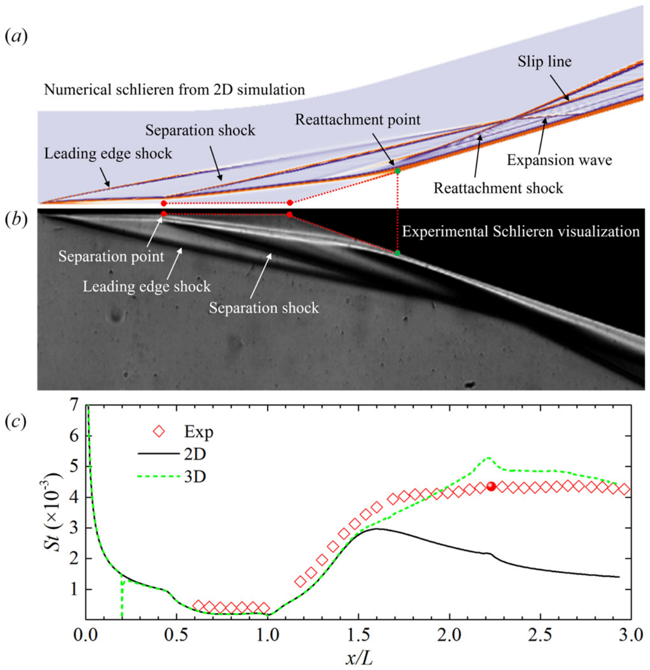

FIG. 2. (a) Two-dimensional numerical schlieren and (b) Experimental schlieren visualization results from Ref. 50. (c) Stanton number distributions along the streamwise direction. Red diamond: Time and spanwise averaged results from Ref. 50. Black solid line: Results obtained from the 2D base flow. Green dashed line: Time and spanwise averaged results from 3D DNS. The largest deviation between the DNS and experimental results occurred in the red stratosphere, where the deviation was approximately 22%.

streamwise direction. Here, $St = \frac{q_w}{\rho_\infty U_\infty C_p (T_{aw}-T_w)}$, q_w denotes the heat flux, C_p is the specific heat capacity and T_{aw} is the adiabatic wall temperature. As shown in Fig. 2(c), the largest deviation between the DNS and experimental results occurred at the red stereosphere, where the deviation was approximately 22 %. According to the heat flux measurement error estimation results of Chuvakhov and Radchenko,[50] the overall error of measurements of the heat flux coefficient was estimated to be about 25 %. This indicates that all the DNS results fall within the error range of the experimental data. The discrepancy between the DNS and experimental results may be attributed to the fact that the environmental disturbance in the experiment was different from the numerical setup in the DNS. Taking such factors into account, the DNS results are considered in reasonably good agreement with the experimental results.

B. Global stability analysis

Figure 3(a) shows the growth rates of the least stable mode as a function of spanwise wavelength λ_z. As evident from Fig. 3(a), the current-incoming flow condition is weakly unstable when the spanwise wavelength $\lambda_z = 19.04$ mm. Figure 3(b) shows the eigenvalue spectrum at $\lambda_z = 19.04$ mm, corresponding to the largest growth rate of the least stable mode. The red circle depicted in Fig. 3(b) demonstrates a growth rate of 0.011. As a result of the low growth rate, it is believed that this case is more susceptible to convective instability than intrinsic instability.

Figures 4(a) and 4(b) show the real parts of streamwise velocity perturbation u' and spanwise velocity perturbation w' of the least stable global mode when $\lambda_z = 19.04$ mm, respectively. The perturbation u' can be detected in both the separation portion and the reattached boundary layer. The distinction lies in the fact that the perturbation w' is predominantly restricted to the separation bubble, with a distinct sign in the upstream and downstream portions of the separation bubble. This type of physical characteristic has been reported by Sidharth *et al.*[63] for hypersonic flow over a slender double wedge and shock impingement on a flat plate investigated by Boin *et al.*,[64] Robinet,[65] and Hildebrand *et al.*[66] The most dominant mode also shares similarities with the self-excited stationary mode detected in an incompressible separation bubble flow identified by Theofilis *et al.*[67]

C. Resolvent analysis

Base-flow solutions are utilized to conduct global resolvent analysis that spans a wide range of spanwise wavelengths and angular frequencies. The non-dimensional spanwise wavelength λ_z/L ranges from 0.00687 ($\beta L = 914.6$) to 0.2 ($\beta L = 31.4$), the corresponding spanwise wavelength λ_z ranges from 0.3435 to 10.0 mm, and $\omega_r L/U_\infty$

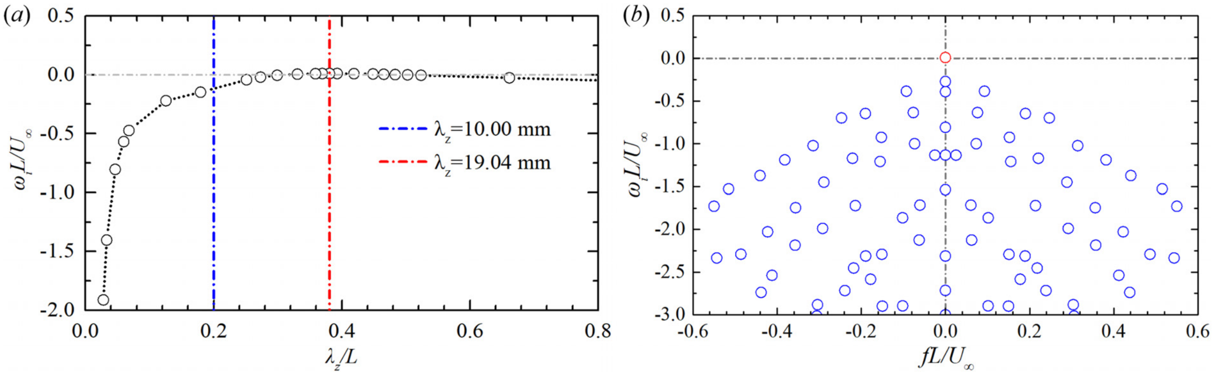

FIG. 3. (a) Growth rates as a function of the spanwise wavelength: The gray short dash-dot line corresponds to a zero growth rate; the short blue dash-dot line represents $\lambda_z = 10.00$ mm; and the short red dash-dot line represents $\lambda_z = 19.04$ mm and (b) Eigenvalue spectrum at $\lambda_z = 19.04$ mm, corresponding to the largest growth rate of the least stable mode. The red circle depicted in Fig. 3(*b*) demonstrates a growth rate of 0.011.

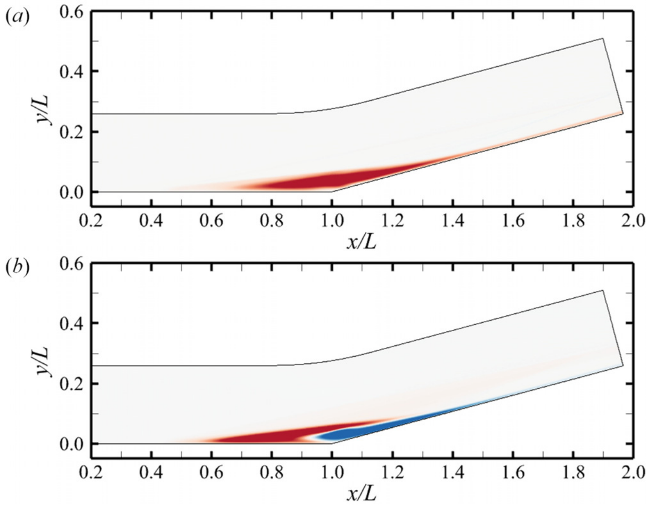

FIG. 4. Real parts of (a) streamwise velocity perturbation u' and (b) spanwise velocity perturbation w' of the least stable global mode at $\lambda_z = 19.04$ mm.

spans the range from 0.1 ($f = 372$ Hz) to 158.5 ($f = 590.3$ kHz). As can be seen in Fig. 3(*a*), in this range of spanwise wavelengths, it has been determined that the base flow is globally stable, thereby enabling the execution of resolvent analysis. It is noteworthy that the forcing is located at $x/L = 0.2$, which is under the subsequent three-dimensional DNS.

The obtained optimal gain is depicted in the β-ω_r space in Fig. 5, the gain is maximal when $\beta L = 195.1$ (λ_z/L=0.0322, λ_z= 1.61 mm), as the frequency $\omega_r L/U_\infty$ is getting close to zero. Actually, when $\omega_r L/U_\infty < 5.5$ ($f < 20.5$ kHz), the optimal gain hardly changes with the forcing frequency. Similar low-pass characteristics were also observed in the study of hypersonic compression-ramp flow by Dwivedi *et al.*[62] and in the investigation of shock impingement on a supersonic boundary layer by Bugeat *et al.*[68] In Fig. 5, an additional local maximum of the optimal gain can be identified on the left edge of the phase diagram of $\beta L = 31.4$ (λ_z/L=0.2) at $\omega_r L/U_\infty \approx 134$, which is marked with a blue circle, and this frequency is approximately 499.05 kHz, corresponding to the Mack second mode. Based on the results of the resolvent analysis, it can be determined that the spanwise length of the subsequent three-dimensional DNS is 16 mm, corresponding to approximately 10 spanwise wavelengths.

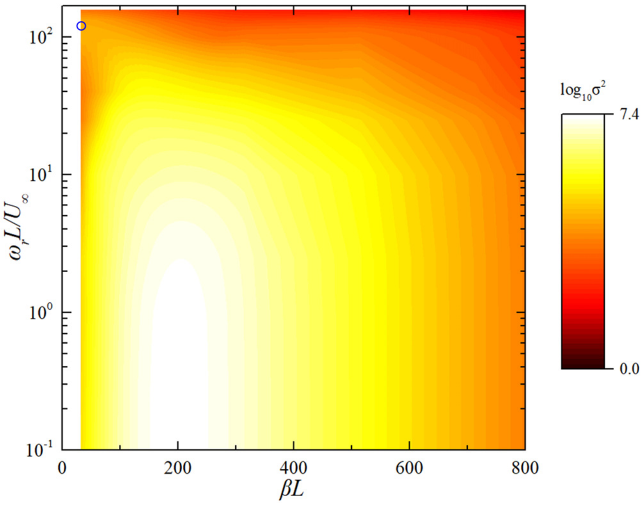

FIG. 5. The contour of optimal gain in the space of spanwise wavenumber and angular frequency. The gain is maximal when $\beta L = 195.1$ (λ_z= 1.61 mm), as the frequency $\omega_r L/U_\infty$ is getting close to zero. In Fig. 5, an additional local maximum of the optimal gain can be identified on the left edge of the phase diagram of $\beta L = 31.4$ (λ_z/L=0.2) at $\omega_r L/U_\infty \approx 134$, which is marked with a blue circle, and this frequency is approximately 499.05 kHz, corresponding to the Mack second mode.

Figure 6 illustrates the most amplified optimal forcing and response pairs when $\omega_r L/U_\infty = 0.1$ and $\lambda_z/L = 0.0322$. The optimal forcing occurs in the form of counter-rotating streamwise vortices ($|u'| \ll |v'|$ and $|u'| \ll |w'|$), whereas the response manifests in the form of streamwise streaks ($|u'| \gg |v'|$ and $|u'| \gg |w'|$, $|v'|$ and $|w'|$ are not shown here). A component-wise energy transfer such as this is usually attributable to the lift-up mechanism,[69] which is held accountable for the transient growth of the streamwise streaks as they traverse the flat plate.

To further illustrate the physical mechanisms that amplify streamwise streaks in the interaction region, the distribution of Chu energy density integrated into the wall-normal direction along the model surface at the most amplified spanwise wavenumber of streaks is shown in Fig. 7(a). The red stereospheres depicted in Fig. 7(a) represent the separation and reattachment points. The growth in energy density is divided into two stages by the separation bubble, and it increases significantly near the separation and reattachment points due to the larger curvatures compared with the shear layer and reattached boundary layer region.[16] The Görtler number can be estimated

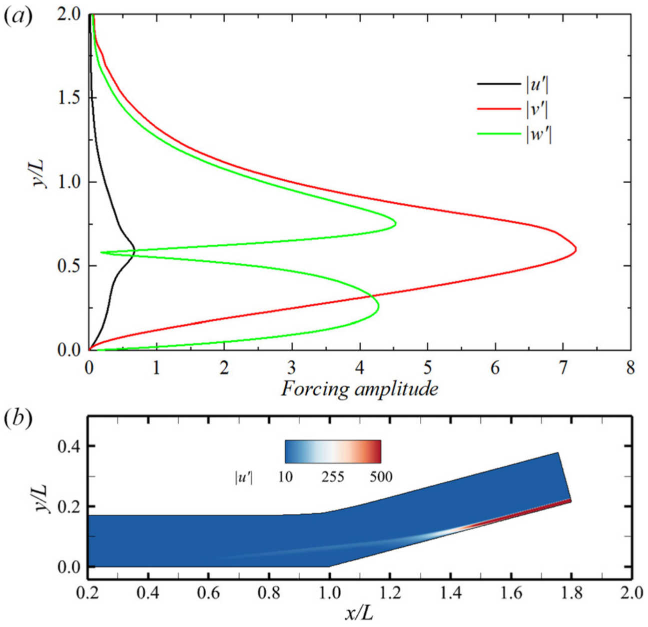

FIG. 6. (a) Optimal forcings and (b) responses associated with the most amplified streamwise streaks at $\omega_r L/U_\infty = 0.1$ and $\lambda_z/L = 0.0322$.

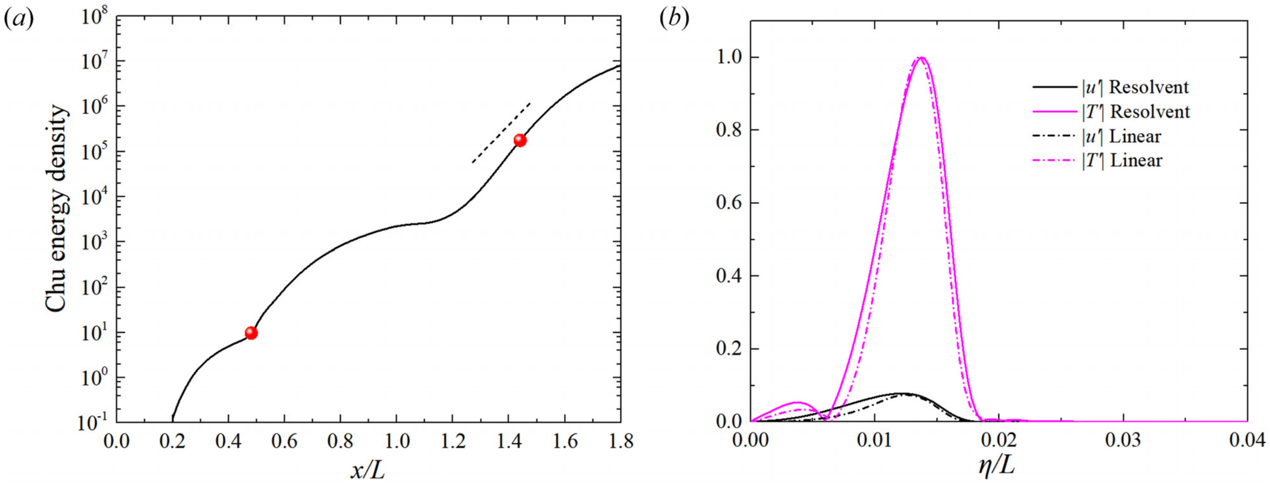

FIG. 7. (a) The distribution of Chu energy density integrated in the wall-normal direction at the most amplified spanwise wavenumber of streaks ($\beta L = 195.1$, $\omega_r L/U_\infty = 10$). The red stereospheres represent the separation and reattachment points. The slope of the short line segment is determined from the spatial growth rate of the most unstable Görtler mode predicted by the linear stability analysis at the reattachment point. (b) Wall-normal distributions of streamwise velocity and temperature perturbations, normalized by the maximum temperature perturbation amplitude at the most amplified spanwise wavenumber, the profiles are exacted at the reattachment point, η is the wall-normal distance from the model surface. Solid lines: Resolvent analysis results. Short dash-dot lines: Linear stability analysis results.

by $G = Re\sqrt{\delta_x/R}$, where $Re = \sqrt{Re_\infty x}$, and $Re_\infty = 7.8 \times 10^6\ \mathrm{m}^{-1}$ is the unit Reynolds number, $\delta_x = \sqrt{x/Re_\infty}$, and R is the radius of curvature. The representative curvature is computed by averaging the curvatures from the wall to the edge of the reattached shear layer near the reattachment point. The resulting curvature is approximately $6.4\ \mathrm{m}^{-1}$, which corresponds to $G = 18.6$. According to Hall[70] and Bottaro and Luchini,[71] local stability analyses can be performed within this range of Görtler's number at this location. Then, linear stability analysis, as detailed in Appendix C, is performed utilizing wall-normal profiles, which are assumed to be parallel along the ξ direction. Here, ξ is the distance along the model surface measured from the leading edge. Due to the strong non-parallelism near the separation point, the wall-normal profile is extracted at the reattachment point. The spatial growth rate obtained from linear stability analysis at the most unstable spanwise wavenumber is converted to the slope of the line segment shown in Fig. 7(a). As seen, the linear stability analysis captures the stationary Görtler mode. Figure 7(b) compares the velocity and temperature perturbations obtained from the resolvent analysis and linear stability analysis at the reattachment point. The magnitude of the temperature perturbation is larger than that of the streamwise velocity perturbation, which is the typical feature of Görtler instability at high Mach numbers. Ren and Fu[72] emphasized this characteristic in their publication. More importantly, the excellent agreement between the local and global analyses confirms that the streamwise streaks are amplified in the interaction region due to the Görtler instability, as the local stability analysis identifies the stationary Görtler mode. Hao *et al.*[16] reached the same conclusion using the resolvent analysis and linear stability analysis under the incoming flow condition at Mach 7.7 (for additional details, refer to Fig. 22 of their paper). This evidence strongly suggests that the streamwise streaks are amplified as a consequence of the Görtler instability. In Fig. 7, the small discrepancies in terms of the eigenfunctions near the wall region and the spatial growth rates may be attributed to the non-parallelism of the base flow.

D. Three-dimensional direct numerical simulation

The initial three-dimensional flow field is constructed as a result of the extension of the two-dimensional base flow along the spanwise direction. Inspired by the research of Hader and Fasel,[73] when detailed information about free-stream perturbations is not readily attainable, random forcing can be utilized to excite broadband upstream disturbances, which makes it possible to investigate the "natural" transition process that was detected in wind tunnel experiments. Random forcing is introduced upstream of the separation point in the current study, taking the following form:

$$w'_{j,k}/U_\infty = \phi_n(2r - 1), \tag{15}$$

where the j and k values correspond to grid point indices along the normal and spanwise directions, respectively. The amplitude of perturbations is represented by ϕ_n, and r denotes a pseudo-arbitrary number that varies from 0 to 1. In this case, random spanwise velocity perturbations with an amplitude of $\phi_n = 0.06$ are imposed on all the grid nodes in the y–z plane at $x/L = 0.2$. The main reasons for the selection of this perturbation amplitude are as follows: First, the transition position and spanwise wavelength obtained from the DNS generated by the selected disturbance amplitude match well with the experimental results. Second, the perturbation of this amplitude can decay rapidly as it propagates downstream on the flat plate. An adequate amount of time is guaranteed for the convection of disturbances through grid points, achieved by updating the perturbation every 50-time steps instead of every time step, which means the spanwise velocity is updated at a time interval of $\Delta t U_\infty/L = 0.002$ ($\Delta t = 8.54 \times 10^{-8}$ s). The data acquisition frequency of DNS is identical to the update frequency of disturbance, namely, the sampling frequency is $f_{\mathrm{sampling}} = 11.71$ MHz. Subsequently, the random forcing and excited perturbations are analyzed by utilizing spectral analysis. When it comes to spectral analysis methods, Welch's method[74] is adopted to calculate the spectrum with three segments and 50% overlap. Before proceeding to the fast Fourier transform procedure, a Hamming window is applied to weigh the data on each segment.

Figure 8(a) provides the temporal history of the spanwise velocity perturbation within the boundary layer at $x/L = 0.2$. As can be seen clearly, random values between -0.06 and 0.06 are introduced at this point. The corresponding PSD results are depicted in Fig. 8(b). As anticipated, the resultant spectrum exhibits broadband characteristics, indicating that the introduction of the disturbance and its subsequent progression are within expectations. The induced pressure disturbance at $x/L = 0.2$ and the corresponding frequency spectrum of this wall pressure signal is depicted in Figs. 8(c) and 8(d). Analogous to the spanwise velocity, the induced pressure disturbances also exhibit a broadband spectrum. This implies that, when utilizing random forcing, we do not settle on a mode with a particular frequency or wavelength but let the flow determine the most preferred mode from the variety of disturbances. This method is suitable for verifying the resolvent analysis results and exemplifies a scenario that is likely to occur during wind tunnel experiments.

As the disturbances are conveyed downstream, they undergo a rapid decay process. The temporal evolution of the spanwise velocity and pressure perturbations at $x/L = 0.3$ is shown in Fig. 9; it is evident that the magnitude of both disturbances decreases dramatically. The blue dashed line depicted in Fig. 9(d) corresponds to the frequency of $f = 400\,\text{kHz}$. This frequency corresponds to the predominant frequency of the Mack second mode instability for the profile of the boundary layer.

1. Comparison between DNS and theoretical predictions

In this section, the laminar and turbulent boundary-layer profiles obtained from DNS are compared with theoretical predictions. By introducing a rescaled wall-normal coordinate, the transformed streamwise velocity profiles at $x/L = 0.4$ and 2.92 are graphically displayed in Fig. 10(a). In this scenario, the streamwise velocity is normalized as:

$$u^+ = \frac{\bar{u}_s}{\bar{u}_\tau}, \tag{16}$$

where $\bar{u}_s$ is the velocity along the wall-parallel direction and $\bar{u}_\tau = \sqrt{\bar{\tau}_w/\bar{\rho}_w}$ denotes corresponding friction velocity. The overline "-" signifies a quantity that has been averaged across both time and spanwise directions. The streamwise velocity is subsequently transformed by executing the Van Driest transformation as a result of the compressibility.

$$u_c^+ = \int_0^{u^+} \sqrt{\frac{\bar{T}_w}{\bar{T}}} du^+. \tag{17}$$

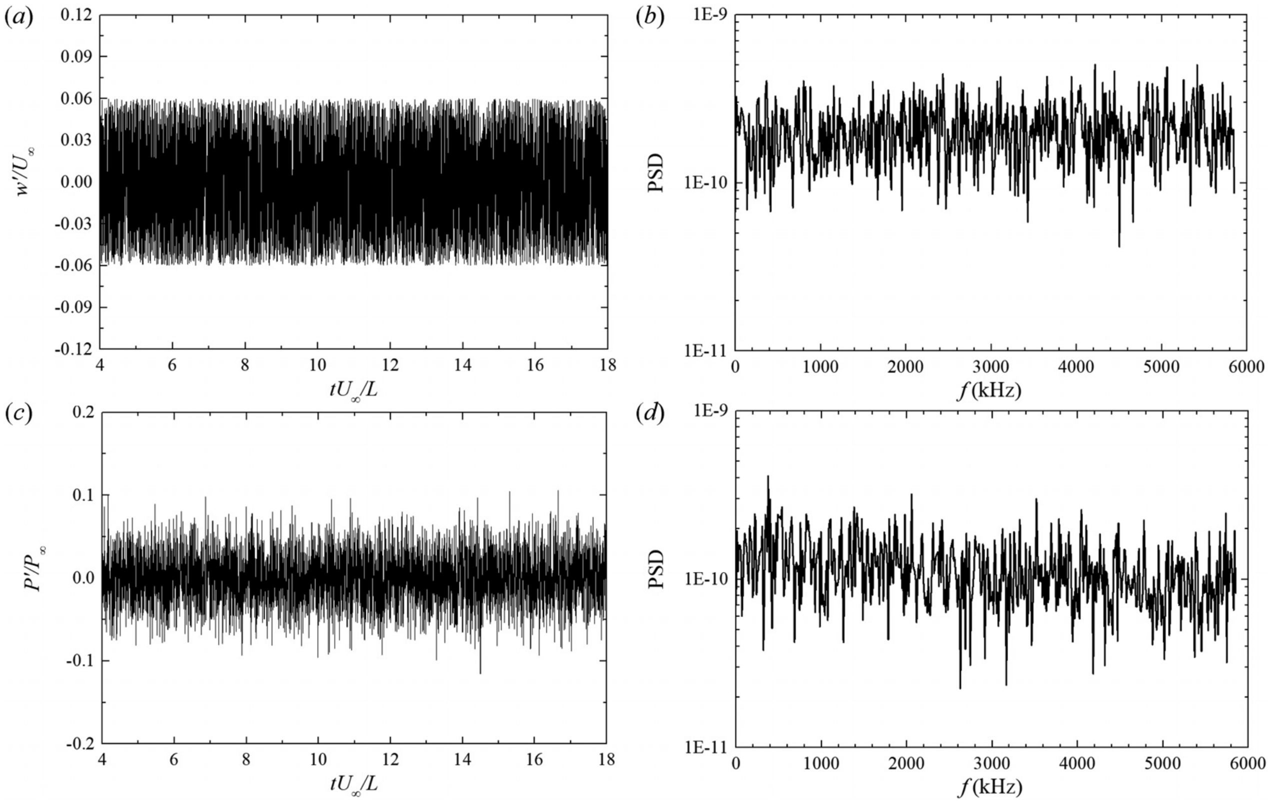

FIG. 8. (a) Temporal history of spanwise velocity perturbation at $x/L = 0.2$ ($j = 45$, $k = 100$). (b) Power spectral density (PSD) results of spanwise velocity time series. (c) Temporal history of pressure perturbation at $x/L = 0.2$ ($j = 1$, $k = 100$). (d) PSD results of pressure perturbation time series.

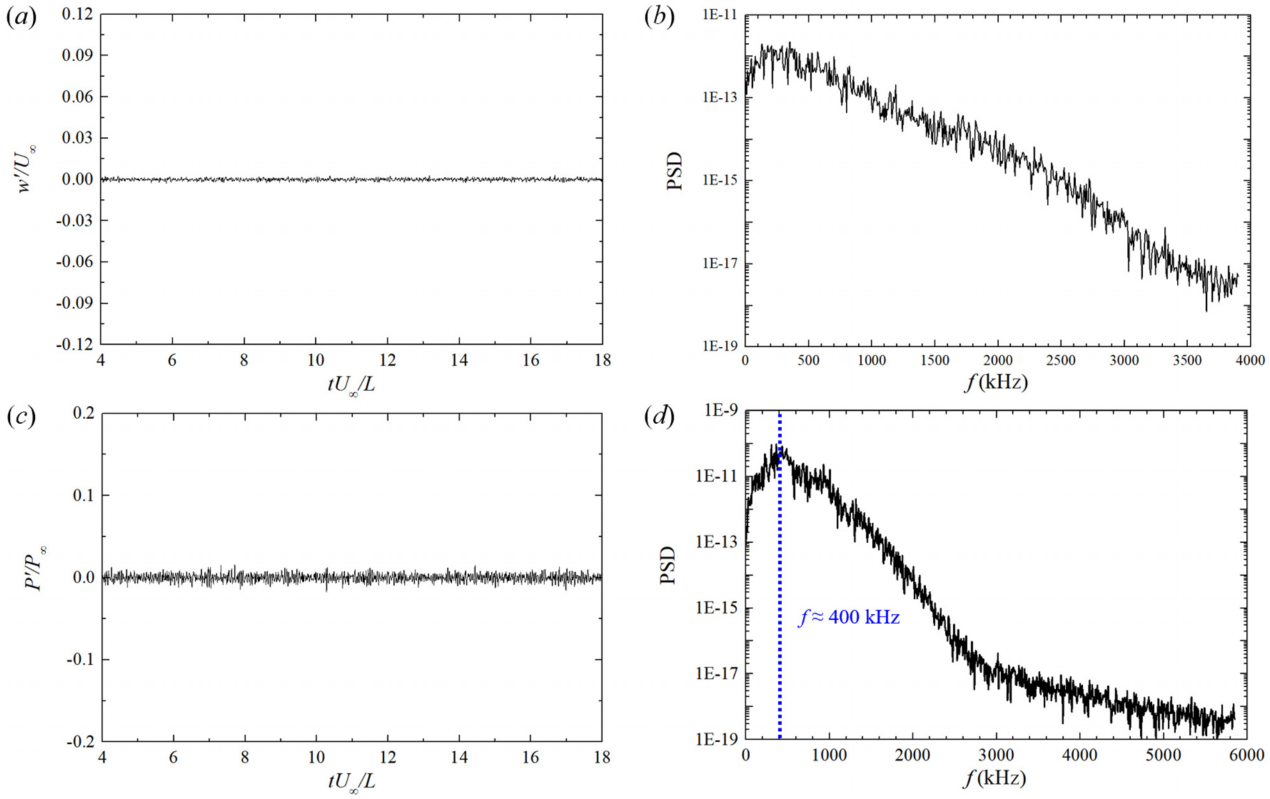

FIG. 9. (a) Temporal history of spanwise velocity perturbation at $x/L = 0.3$ ($j = 45$, $k = 100$). (b) PSD results of spanwise velocity time series. (c) Temporal history of pressure perturbation at $x/L = 0.3$ ($j = 1$ and $k = 100$). (d) PSD results of pressure perturbation time series. The blue dashed line depicted in Fig. 9(d) corresponds to the frequency of $f = 400$ kHz (the Mack second mode).

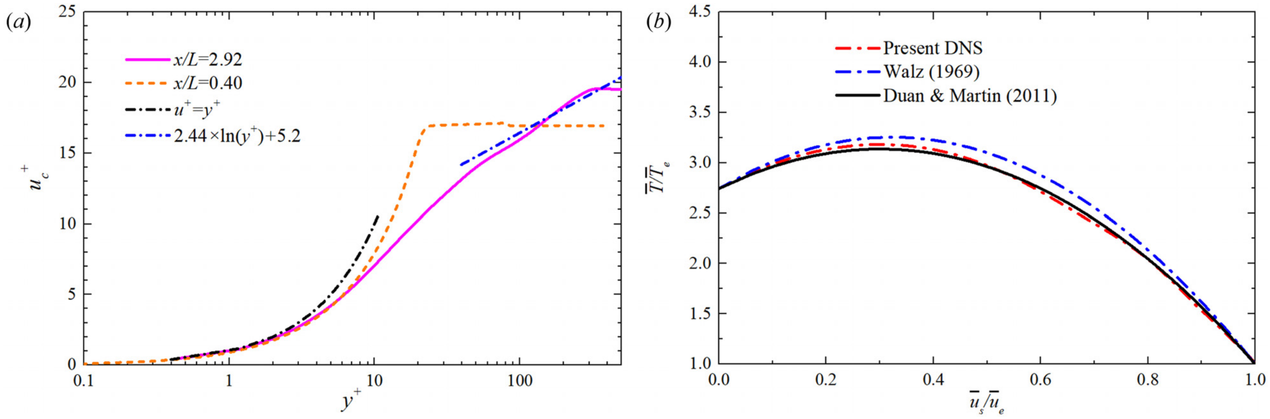

FIG. 10. (a) The van-Driest-transformed mean velocity profile at $x/L = 0.4$ and 2.92. The short black and blue dashed dot lines represent linear sublayer and log-law relations, respectively. (b) The mean temperature profile at $x/L = 2.92$ compared with the relations proposed by Walz in Ref. 76 and Duan & Martin in Ref. 77.

In Fig. 10(a), the short black and blue dashed dot lines represent linear sublayer and log-law relations, respectively.

$$u^+ = y^+, \tag{18}$$

$$u^+ = \frac{1}{k}\ln(y^+) + C, \tag{19}$$

where $k = 0.41$ and $C = 5.2$. The velocity profile exhibits the typical characteristics of a laminar profile at $x/L = 0.4$. When $x/L = 2.92$, the associated velocity distribution demonstrates the typical characteristics of a turbulent boundary layer. It should be noted that the linear relation $u^+ = y^+$ is satisfied only when y^+ is less than 2 in the viscous sublayer region. This scenario is similar to that of Duan *et al.*,[75] who studied Mach 5 turbulent boundary layers on a cold wall case and demonstrated that the viscous sublayer shrinks substantially in response to decreasing wall temperature. The primary contributing factor to the aforementioned phenomenon lies in the low ratio of wall temperature to total temperature. When y^+ does not exceed 10, the velocity profile at $x/L = 3.0$ coincides with that of the laminar flow, which indicates that the viscous sublayer is solved precisely. Furthermore, the velocity profile in the logarithmic region agrees well with the theoretical prediction.

The subsequent step involves comparing the temperature profile with the theoretical solution. The temperature profile that has been averaged across time and spanwise direction at $x/L = 2.92$ is depicted in Fig. 10(b). The commonly used one is the relation between temperature and velocity, expressed by Walz's equation,[76] shown below:

$$\frac{\bar{T}}{\bar{T}_e} = \frac{\bar{T}_w}{\bar{T}_e} + \frac{\bar{T}_{aw} - \bar{T}_w}{\bar{T}_e}\left(\frac{\bar{u}_s}{\bar{u}_e}\right) + \frac{\bar{T}_e - \bar{T}_{aw}}{\bar{T}_e}\left(\frac{\bar{u}_s}{\bar{u}_e}\right)^2. \tag{20}$$

As evident from Fig. 10(b), the DNS results do not coincide well with the corresponding result of Walz's relation, as it was originally proposed based on the boundary layer over an adiabatic wall. Duan and Martin[77] proposed a novel relation based on Walz's equation, considering the influence of the cold wall effect.

$$\frac{\bar{T}}{\bar{T}_e} = \frac{\bar{T}_w}{\bar{T}_e} + \frac{\bar{T}_{aw} - \bar{T}_w}{\bar{T}_e} f\left(\frac{\bar{u}_s}{\bar{u}_e}\right) + \frac{\bar{T}_e - \bar{T}_{aw}}{\bar{T}_e}\left(\frac{\bar{u}_s}{\bar{u}_e}\right)^2. \tag{21}$$

where $f\left(\frac{\bar{u}_s}{\bar{u}_e}\right)$ is expressed as follows:

$$f\left(\frac{\bar{u}_s}{\bar{u}_e}\right) = 0.1741\left(\frac{\bar{u}_s}{\bar{u}_e}\right)^2 + 0.8259\left(\frac{\bar{u}_s}{\bar{u}_e}\right). \tag{22}$$

As depicted in Fig. 10(b), the present DNS result is in good concordance with the modified relation proposed by Duan and Martin.[77] It signifies that the current DNS is capable of accurately solving the velocity and temperature fields in the laminar and full turbulent regions, and it is in good agreement with theoretical predictions. This affirms the accuracy of the DNS results, thereby enabling further analysis in the next step.

2. Spanwise wavelength

Figure 11 presents the instantaneous wall Stanton number distribution at $tU_\infty/L = 4.8$, 11.2, and 19.2, as well as the time-averaged wall Stanton number distribution, in which the superimposed black solid lines represent the zero-skin friction $C_f = 0$ locations. As can be seen, strong three-dimensionality can be observed along the spanwise direction at different time levels, and transition phenomena occur not far away from the reattachment line, which will be analyzed later.

For the analysis of spanwise wavelengths, Fig. 12 illustrates the heat-flux streaks on the ramp surface by comparing the temperature-sensitive paint image from Chuvakhov and Radchenko *et al.*[50] and the numerical Stanton number map. Additionally, the gain derived from resolvent analysis as a function of spanwise wavelength at $\omega_r L/U_\infty = 0.1$, along with spanwise wavelengths derived from the three methods, is also shown in Fig. 12(c). The spanwise wavelength estimated by the experiment spans from 1.58 to 3.9 mm, while the spanwise wavelength obtained by the DNS is about 1.6 mm. As previously mentioned, the spanwise wavelength obtained from the resolvent analysis is 1.61 mm, indicating that the spanwise wavelengths obtained from DNS and resolvent analysis fall within the range of experimental results. The perfect alignment of spanwise wavelengths obtained using three distinct approaches suggests that the transition phenomenon corresponding to current incoming flow conditions is primarily dominated by convective instabilities.

3. Transition position

In this section, the vortex structure and the corresponding transition position will be analyzed. The *Q*-criterion, also frequently referred to as the second invariant of the velocity gradient tensor, is a method adopted for vortex identification and visualization in fluid dynamics. Here, it is used to identify the vortex structures in the boundary layer of the current hypersonic compression flow. Figure 13 shows the instantaneous visualization of the vortex structure utilizing the

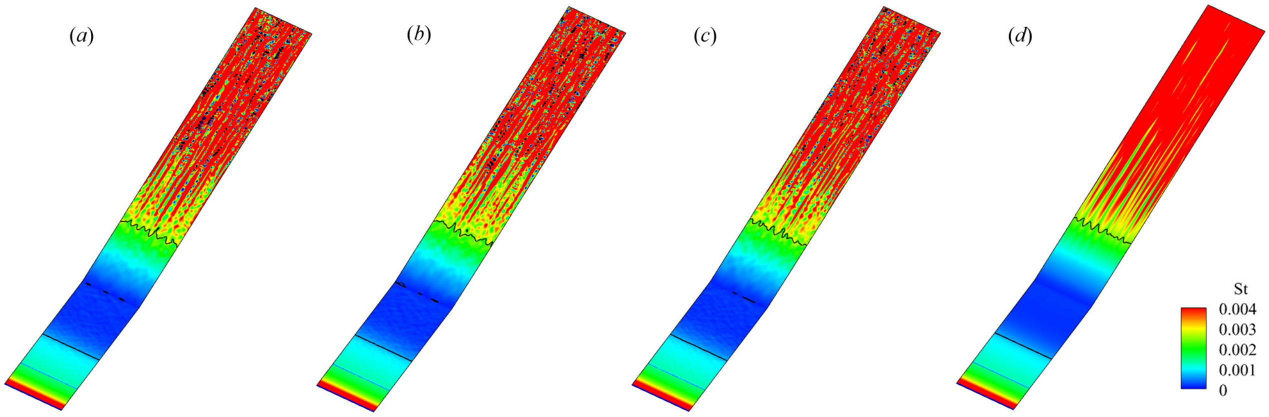

FIG. 11. Instantaneous wall Stanton number distribution at (*a*) $tU_\infty/L = 4.8$, (*b*) $tU_\infty/L = 11.2$, (*c*) $tU_\infty/L = 19.2$, and (*d*) Time-averaged wall Stanton number distribution. The black solid lines denote the iso-lines of $C_f = 0$.

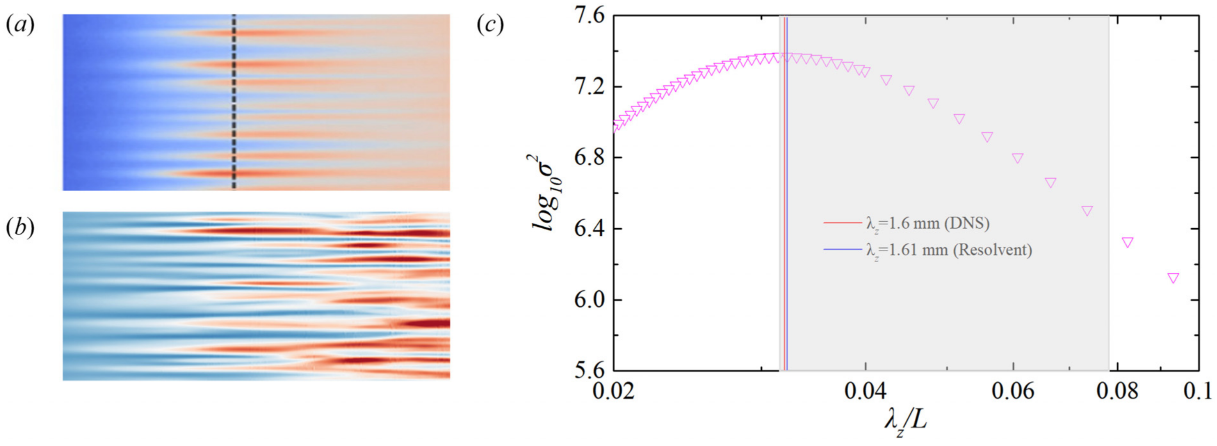

FIG. 12. (a) The temperature-sensitive painting image from Ref. 50 and (b) the numerical Stanton number map illustrates the heat-flux streaks on the ramp surface. Figures 12(a) and 12(b) are both time-averaged results. (c) The gain derived from resolvent analysis as a function of spanwise wavelength at $\omega_r L/U_\infty = 0.1$, along with spanwise wavelengths derived from three methods. Here, the log coordinate is used for the abscissa. Gray rectangular window: Spanwise wavelength range of experimental results; Red solid line: DNS results; Blue solid line: Resolvent analysis results.

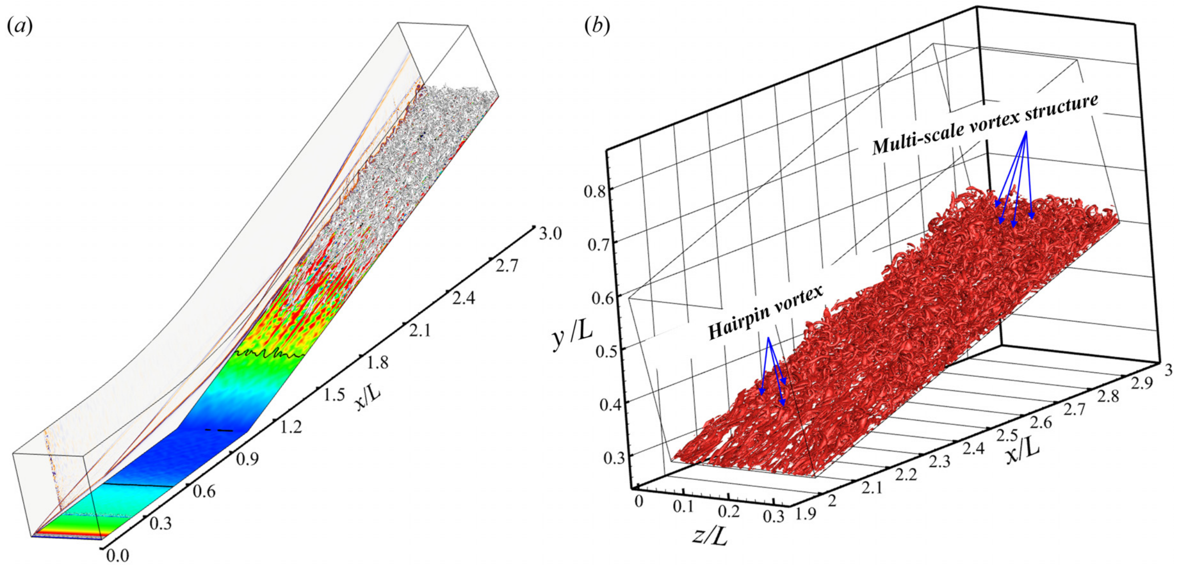

FIG. 13. (a) Instantaneous visualization of the vortex structure utilizing the Q-criterion at $tU_\infty/L = 19.2$. Stanton number is shown together with isolines of zero skin friction coefficient. The numerical schlieren is additionally added to emphasize the separation bubble and shock system. (b) An enlarged view of Fig. 13(a) in transitional and full turbulence regions. The iso-surface of $Q = 100$, is depicted in both sub-FIGS.

Q-criterion at $tU_\infty/L = 19.2$. As can be seen from Fig. 13(a), the vortex structure evolved along the streamwise direction downstream of the reattachment line. The typical hairpin vortex structures appeared in the transitional region and then gradually developed into multiscale vortex structures, forming fully developed turbulence flow. It is evident from Fig. 13(b) that in the region spanning from $x/L = 2.0$ to $x/L = 2.3$, the typical hairpin vortex structures start to appear, corresponding to the position where the transition commences. Downstream of $x/L = 2.3$, multiscale vortex structures formed, which indicates that a fully developed turbulent flow is formed. Thereafter, possible transition mechanisms will be put forward.

IV. POSSIBLE TRANSITION MECHANISMS

To unveil the unstable modes that dominate the transition process, Fig. 14 shows the temporal history of fluctuations in temperature, density, spanwise velocity, and pressure at $x/L = 1.77$ $(j = 10, k = 100)$, as well as the PSD results of corresponding signals. In Figs. 14(b), 14(d), 14(f), and 14(h), the red and blue dashed lines correspond

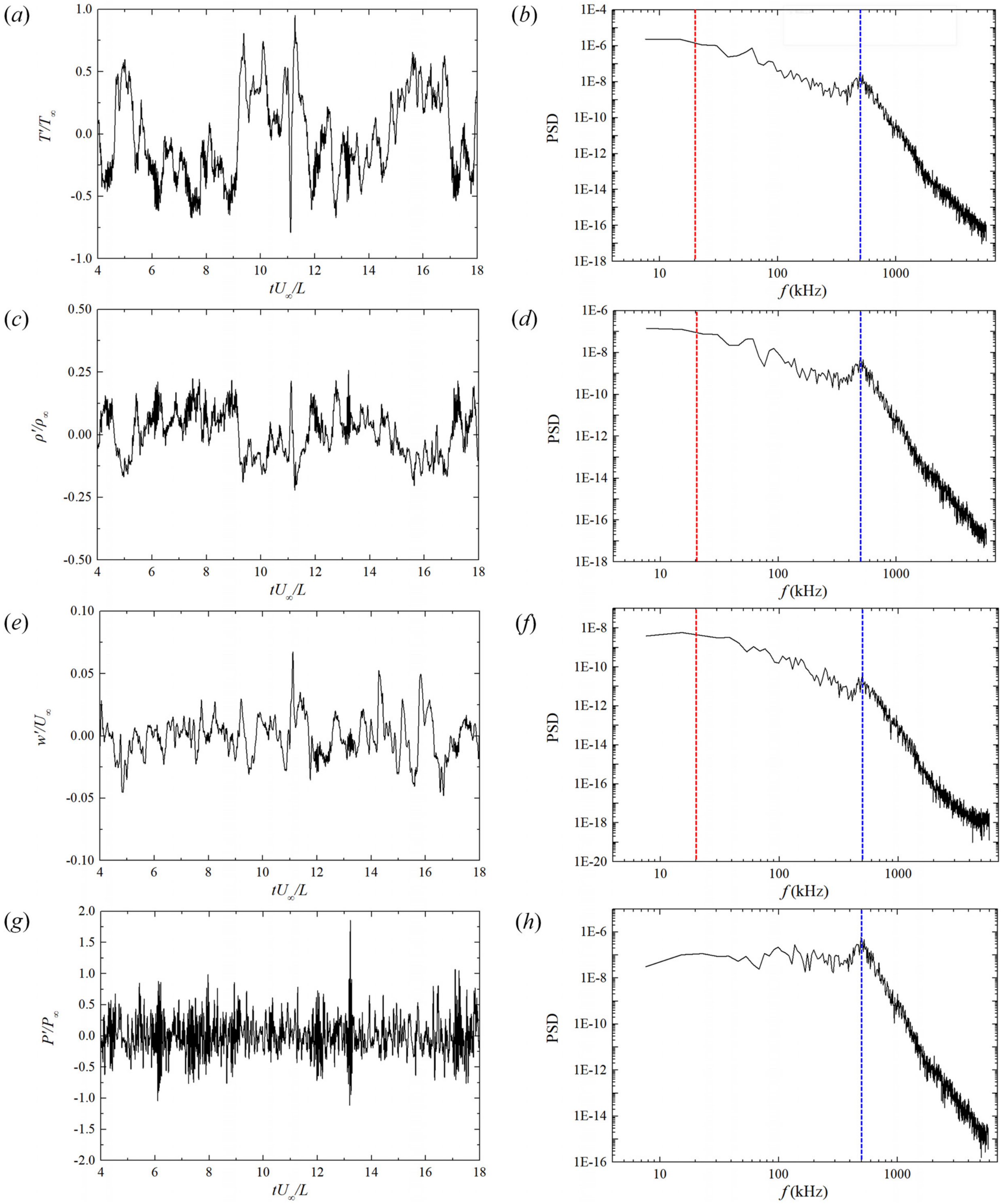

FIG. 14. (a) Temporal history of temperature fluctuation at $x/L = 1.77$ ($j = 10$, $k = 100$), (b) PSD of the signal in (a), (c) temporal history of density fluctuation at $x/L = 1.77$ ($j = 10$ and $k = 100$), (d) PSD of the signal in (c), (e) temporal history of spanwise velocity fluctuation at $x/L = 1.77$ ($j = 10$ and $k = 100$). (f) PSD of the signal in (e). (g) Temporal history of pressure fluctuation at $x/L = 1.77$ ($j = 10$ and $k = 100$). (h) PSD of the signal in (g). The red and blue dashed lines correspond to $f \approx 20.5$ kHz (low-frequency streaks mode) and $f \approx 500$ kHz (the Mack second mode), respectively.

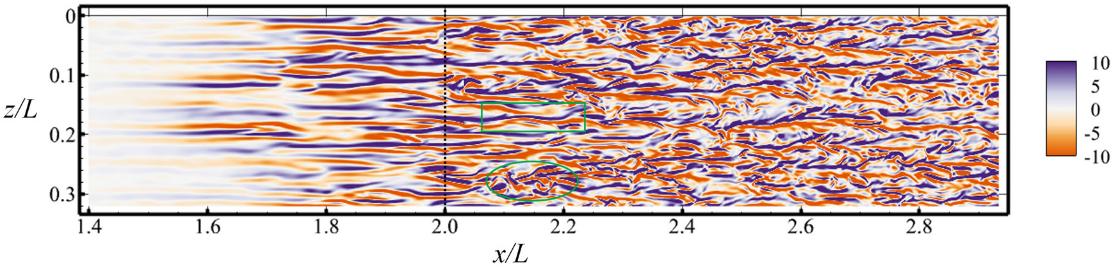

FIG. 15. Instantaneous distribution of the non-dimensional streamwise vorticity on the wall-parallel plane at $y_n/L = 0.006$ ($tU_\infty/L = 19.2$). The black dot line ($x/L = 2.0$) in the contour indicates the position where the streamwise vortex begins to bifurcate and break down. The green rectangle and ellipse denote the sinuous (odd) mode and varicose (even) mode, respectively.

to $f = 20.5$ and 500 kHz, respectively. Regarding the two predominant frequencies, $f = 20.5$ kHz pertains to the dominant frequency of low-frequency streaks mode, whereas $f = 500$ kHz corresponds to the dominant frequency of the Mack second mode. From Figs. 14(b), 14(d), and 14(f), the energy amplitude associated with Mack's second mode is lower than that associated with the low-frequency streaks mode, indicating that the streaks exert a significant impact on the transition process. However, as can be observed from Fig. 14(h), the second mode also plays a prominent role in the fluctuation of the pressure signal. The aforementioned findings strongly suggest that both streaks and Mack's second mode play a substantial role in the transition burst process. However, the specific role of these two modes in transitions under the current flow condition is still unclear, so further analysis is necessary.

In compression ramp flows, streaks that appear near the reattachment are generally considered to be the footprint of Görtler-like vortices, and such streaks tend to have spanwise-periodic and streamwise-elongated features. To further explicate the role of the low-frequency streaks mode during the transition process, Fig. 15 depicts the instantaneous distribution of the non-dimensional streamwise vorticity on the wall-parallel plane at $y_n/L = 0.006$ ($tU_\infty/L = 19.2$), and Fig. 16 presents the corresponding instantaneous streamwise velocity distributions along different y-z planes within boundary layers. Note that y_n in Figs. 15 and 16 denotes the wall-normal coordinate that starts from the wall.

It is well-illustrated that streak-like structures are the most typical features in boundary layer transition flows caused by Görtler instability. As shown in Fig. 15, upstream of $x/L = 2.0$, such streaks exhibit clear streamwise-elongated features. Moreover, from Figs. 16(a)–16(d), i.e., from $x/L = 1.57$ to $x/L = 2.0$, the interface between the boundary layer and the mainstream gradually evolves from flat to meandering. In particular, at $x/L = 2.0$, boundary layers arch upward and gradually form weak plume-like structures. The aforementioned evidence signifies that as the boundary layer develops downstream, the boundary layer is destabilized,Görtler instability may play a pivotal role in the formation and evolution of streamwise vortices in the current compression ramp flow.

As the boundary layer flows further downstream, as highlighted in Fig. 15, downstream of $x/L = 2.0$, a single streak, it bifurcates into multiple branches, and those streak structures lose their original regular shape along the streamwise direction, gradually becoming chaotic. Such evolutionary features can be sustained up to $x/L \approx 2.3$. In this

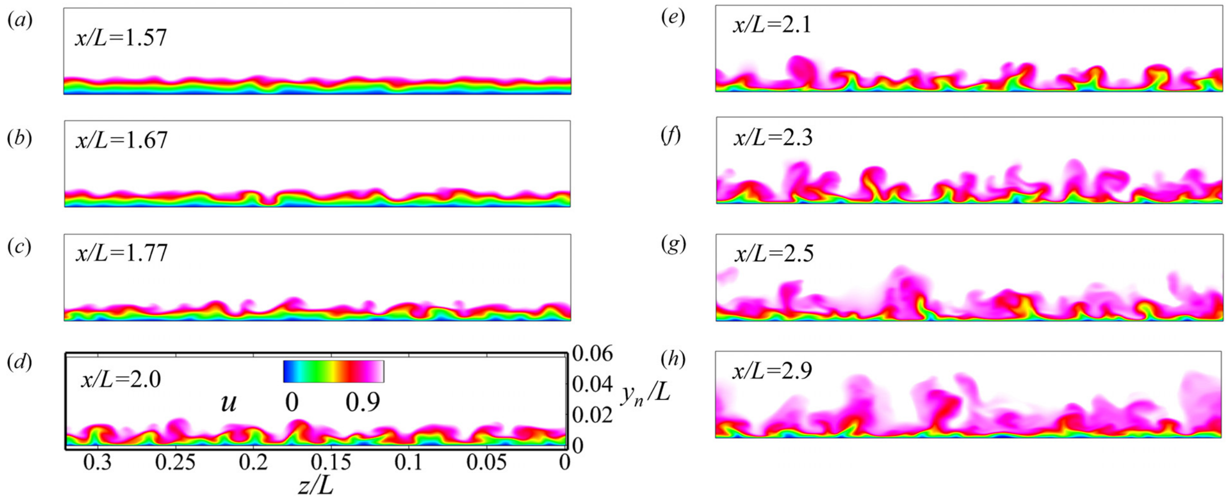

FIG. 16. Instantaneous streamwise velocity distributions along different y-z planes within boundary layers at $tU_\infty/L = 19.2$. (a) $x/L = 1.57$, (b) $x/L = 1.67$, (c) $x/L = 1.77$, (d) $x/L = 2.0$, (e) $x/L = 2.1$, (f) $x/L = 2.3$, (g) $x/L = 2.5$, and (h) $x/L = 2.9$.

region, the sinuous and varicose modes coexist in the current flow condition, which is depicted with a green rectangle and an ellipse in Fig. 15. The two observed patterns bear resemblance to those frequently reported in the literature pertaining to Görtler instability.[78,79] For instance, Hall *et al.* performed an analytical examination of the boundary layer flow over a curved wall and identified two distinct modes during the breakdown scenario of Görtler vortices, namely the odd and even modes.[80] Li and Malik further revealed that the sinuous shape of Görtler vortices is initiated by the odd mode, whereas the even mode results in a varicose shape.[79] Such similarity suggests that Görtler instability may play an important role in the bifurcation and breakdown of low-frequency streaks. This process is depicted in Fig. 16(d) (i.e., $x/L = 2.0$) to Fig. 16(f) (i.e., $x/L = 2.3$), where the outer layer of boundary layers becomes more and more meandering, and the roll-up process of streamwise vortices becomes increasingly noticeable, and such boundary layer morphology embodied in this process indicates that the flow is in a transitional state. Further downstream, the streamwise streaks break down into multi-scale vortex structures and form a fully developed turbulent flow.

As illustrated in Figs. 15 and 16, the role of low-frequency streaks in transition events is intuitive, but the role of the Mack second mode in destabilizing the flow and triggering a laminar-turbulent transition in high Mach number flows is also nonnegligible [refer to Fig. 14(h)]. Figure 17 provides the temporal history of wall pressure at different streamwise locations (i.e., $x/L = 1.47$, 1.57, 1.77, and 1.90) downstream of the reattachment line. It is evident from these figures that the wall pressure signals exhibit a wave-like form, referred to as the Mack second mode [see also Figs. 14(g) and 14(h)]. As can be seen from Figs. 17(a)–17(d), the amplitude of the wall pressure signal gradually increases during its downstream propagation. Specifically, at $x/L = 1.9$, the pressure signal is characterized by high amplitude fluctuations, and its waveform tends to become irregular, indicating that the breakdown scenario will be reached shortly downstream of $x/L = 1.9$. It has already been mentioned that the position at which the transition commences is $x/L = 2.0$, which is consistent with the conclusions drawn here.

To provide more comprehensive spatial information on the current transitional flow, Fig. 18 presents the contours of the vorticity magnitude in the x–y plane at $z/L = 0.08$ ($tU_\infty/L = 19.2$). In circumstances where the amplitude of the pressure signal is small (see Fig. 17 at $x/L = 1.47$ and $x/L = 1.57$), the edge of the boundary layer remains flat until $x/L \approx 1.6$ [see Fig. 18(a)]. When its amplitude further increases, the interface between the boundary layer and mainstream develops a wave-like structure [see Fig. 18(a) at $x/L \approx 1.9$]. Further downstream, the amplification of the Mack second mode, the sinuous and varicose breakdown of streaks, disrupts the boundary layers by ejecting low-momentum fluid upward from the lower portion of the boundary layers [see Fig. 16(e)]. According to mass conservation, high-momentum fluid in the outer layer will sweep downward, resulting in the formation of a localized three-dimensional high-shear layer at the edge of boundary layers, and that is the so-called ejection-sweep motion in boundary layer flows. The ejection-sweep motion creates a strong localized vorticity region that contributes to the concentration of vorticity within the boundary layers, which kicks off the vortex roll-up process ($x/L \approx 2.1$). This vortex roll-up phenomenon is clearly illustrated in Fig. 18(b).

Upon the progression of the vortex roll-up in the high-shear region of the boundary layers, the vortex will undergo distortion and

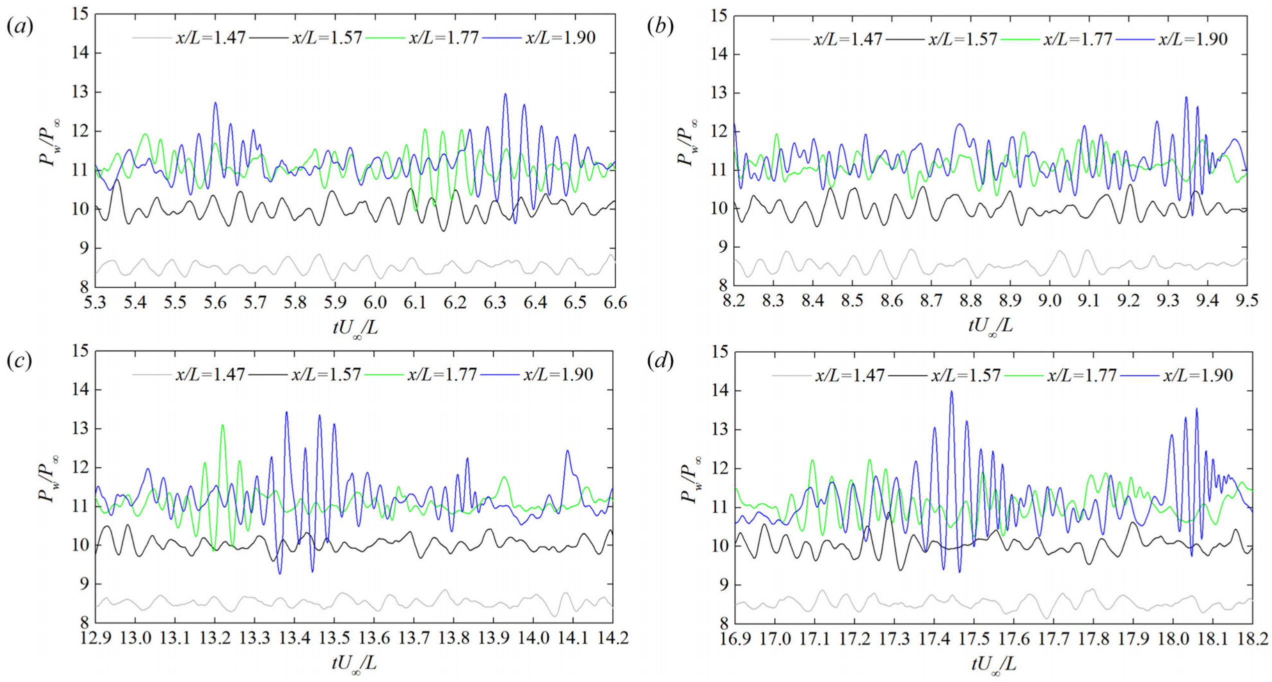

FIG. 17. Temporal history of wall pressure at x/L=1.47, 1.57, 1.77, and 1.90 ($j = 1$, $k = 100$). (*a*) $tU_\infty/L = 5.3 \sim 6.6$, (*b*) $tU_\infty/L = 8.2 \sim 9.5$, (*c*) $tU_\infty/L = 12.9 \sim 14.2$, and (*d*) $tU_\infty/L = 16.9 \sim 18.2$.

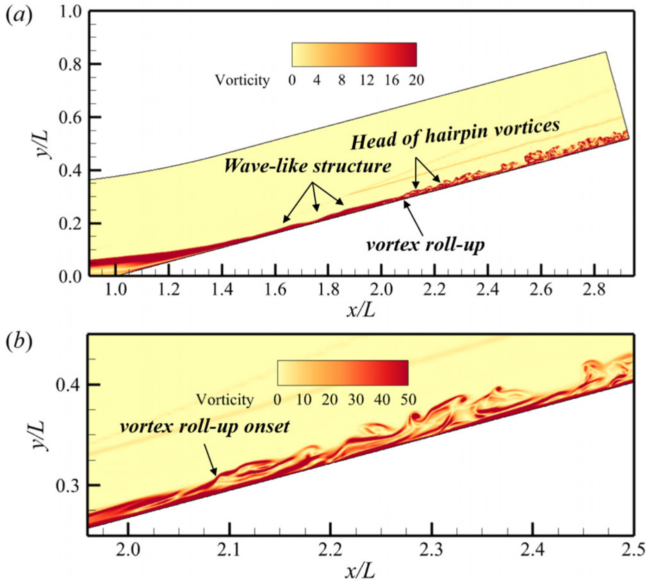

FIG. 18. The contours of the vorticity magnitude in the x–y plane at $tU_\infty/L = 19.2$: (a) $z/L = 0.08$. (b) Enlarged view of Fig. 18(a).

be stretched into a hairpin vortex (see Fig. 18(b) at $x/L \approx 2.2$). During this event, the Mack second mode and streaks play an active role in the maturation of the vortex roll-up process within the boundary layers and thereby contribute to the generation of hairpin vortices. Ultimately, boundary layers break down into multiscale vortex structures within a very short distance, specifically after $x/L \approx 2.3$. It continues to develop downstream, forming a fully developed turbulent flow. In this regard, the amalgamation of the amplification of Mack's second mode with the sinuous and varicose breakdown of streaks results in the formation of hairpin vortices, ultimately leading to the laminar-turbulent transition.

Thus far, it is worth examining whether the initiation of streaks is independent of the Mack second mode, as there are some studies on whether the Mack second mode initiates streaks without the Görtler mechanism. Gray[81] conducted experiments in the Boeing/AFOSR Mach-6 Quiet Tunnel on sharp, slender straight cones at a zero-degrees angle of attack. These long modes allow the second mode to grow to large amplitudes without the need for introduced perturbations and without the presence of the Görtler instability. The doctoral dissertation held that flared cone geometries had previously produced heating streaks. If streaks are also present on the straight cone, it can be confirmed that they are not the result of the Görtler instability over a concave surface, but rather a consequence of the second mode. The experimental results of this doctoral dissertation indeed confirm these conclusions. This hypothesis is further supported by how suppressed the streaks appear on a geometry that suppresses the second mode prior to the separation bubble. For instance, Benitez *et al.*[82] found that the initial expansion corner dampens the second mode under a cone-cylinder flare configuration. Meanwhile, the streaks generated downstream of reattachment are not immediately apparent in the heat flux data until that data is significantly post-processed. Cone flares that have been run at similar conditions, however, have obvious streaks but also do not suppress the second mode. Such evidence signifies that the initiation of streaks is more related to the second mode under their experimental setup. Nevertheless, under the current compression ramp configuration at Mach 8.0, as discussed earlier, from Figs. 14(b), 14(d), and 14(f), the energy amplitude associated with Mack's second mode is lower than that associated with the low-frequency Görtler mode immediately downstream of reattachment, indicating that the streaks are more related to the Görtler instability. As the flow develops further downstream, it can be seen from Fig. 17 that the second mode is continuously amplified. It signifies that, at the late stage of the laminar-turbulent transition, the second mode may initiate streaks through the nonlinear interaction and become involved in the breakdown scenario. In this particular scenario, it presents a challenge to distinguish between the quantitative role of the Mack second mode and the Görtler mechanism in the initiation of streaks, which remains a pending issue warrants further investigation.

Given the coexistence of the Mack second mode and the low-frequency streaks in the flow field, it is natural to consider whether the Mack second mode and the sinuous and varicose modes will interact with one another. Recently, certain researchers have conducted investigations pertaining to the interactions among diverse modes. Chen *et al.*[83] investigated the interactions between the Mack second mode and low-frequency waves in a hypersonic boundary layer. Their findings indicate that the low-frequency modes associated with the unsteady Görtler vortices, with frequencies below approximately 30 kHz, are the most prominently promoted. Song *et al.*[84] studied the secondary instability of stationary Görtler vortices originating from the first/second Mack mode. As they pointed out, once the Görtler vortices have reached a noticeable amplitude within boundary layers, along the spanwise direction, low- and high-speed streaks will form. Such streaks are incapable of breaking down themselves, but they are highly unstable to high-frequency perturbations, which are typically referred to as the secondary instability (i.e., sinuous and varicose modes), and the experimental work of and Blackwelder[85] has confirmed the existence of the secondary instabilities. This signifies that the Mack second mode may play a role in the evolution of the low-frequency streaks as well as the sinuous and varicose modes. Hofferth *et al.*[86] performed a bicoherence analysis and focused schlieren measurements with a flared cone at Mach 6. They not only observed the self-interactions of the Mack second mode, but they also captured the interactions between low-frequency disturbances and the second mode. Ren *et al.*[87] found that, when the amplitude of streaks is large enough to modulate the laminar boundary layer but low enough to not trigger secondary instabilities, the Mack second mode can be effectively suppressed. It is no coincidence; that Huang[43] investigated the interactions between Görtler vortices and the Mack second mode experimentally to determine the influence of Görtler vortices on the second mode. Their findings provide compelling evidence that Görtler vortices exert a stabilizing effect on the Mack second mode when the appropriate amplitude is chosen. This further affirms that there may be interactions between the various modes, including, undoubtedly, the Mack second mode and the low-frequency streak mode. Although studies of the interaction between diverse modes have made significant progress, the quantitative mechanism of interactions between the Mack second mode and sinuous/varicose modes, as well as their potential impacts on transition, remains a pending issue that warrants further investigation.

As there may be multiple possible transition paths to turbulence in hypersonic flows, inevitably, under the current inflow conditions at Mach 8, the transition mechanism aforementioned is a potential explanation based on the current transition phenomenon. Standing on the shoulders of giants, we speculate that there may be interactions between the Mack second mode and sinuous/varicose modes. However, it is imperative to provide robust evidence in future research to clarify the impact of secondary instabilities and the interactions between diverse modes on transition mechanisms.

V. CONCLUSIONS

In this study, global stability analysis and resolvent analysis, as well as DNS, were performed to investigate the stability of hypersonic flow over a compression ramp, and the corresponding free-stream Mach number and Reynolds number are 8.0 and 3.9×10^5, respectively. First, the intrinsic instability was determined by the global stability analysis, it is shown that the current flow condition is weakly unstable. As a result of the low growth rate, this case is believed to be more susceptible to convective instability than intrinsic instability.

Subsequently, across a wide range of frequencies and a globally stable wavelength, resolvent analysis is utilized to investigate the response of two-dimensional base flow to external disturbances that are harmonic in time and the spanwise direction. It reveals that the optimal response to upstream disturbances located adjacent to the leading edge manifests in the form of low-frequency streamwise streaks, which result from transient growth in the flat-plate boundary layer.

Within the boundary layer, the PSD results from the temporal history of fluctuations in temperature, density, spanwise velocity, and pressure at $x/L = 1.77$ reveals two dominant frequencies. Of the two predominant frequencies, $f = 20.5$ kHz pertains to the dominant frequency of the low-frequency streak mode, whereas $f = 500$ kHz corresponds to the dominant frequency of the Mack second mode. The PSD results strongly indicate that both streaks and the Mack second mode play a substantial role in the transition burst process. Further downstream, the amalgamation of the amplification of Mack's second mode with the sinuous and varicose breakdown of streaks disrupts the boundary layers via the ejection-sweep motion, resulting in the creation of a strong localized vorticity region and contributing to the concentration of vorticity within the boundary layers. It kicks off the vortex roll-up process, results in the formation of hairpin vortices, and eventually leads to the breakdown process.

Due to the existence of various forms of disturbance under actual flight conditions, the transition process of the boundary layer may have the coexistence of multiple unstable modes, such as Mack first/second mode instability, crossflow instability,[88] Görtler instability, and nonlinear coupling of different processes. Hence, the transition mechanism proposed in this paper is merely a potential explanation and a more comprehensive examination of the contribution of secondary instabilities and the interactions between the Mack second mode and sinuous/varicose modes to the transition mechanism is imperative, which merits further investigation.

ACKNOWLEDGMENTS

This work was supported by the National Natural Science Foundation of China (Grant Nos. 12302304 and 12102377) and Hong Kong Research Grants Council (Grant Nos. 15204322, 15217622 and 25203721).

AUTHOR DECLARATIONS

Conflict of Interest

The authors have no conflicts to disclose.

Author Contributions

Changye Huang: Conceptualization (equal); Data curation (equal); Formal analysis (equal); Investigation (equal); Methodology (equal); Validation (equal); Visualization (equal); Writing – original draft (equal); Writing – review & editing (equal). **Shibin Cao:** Conceptualization (equal); Funding acquisition (lead); Methodology (equal); Resources (lead); Software (equal); Supervision (lead); Writing – review & editing (equal). **Jiaao Hao:** Conceptualization (equal); Funding acquisition (equal); Methodology (equal); Resources (equal); Software (equal); Supervision (equal); Writing – review & editing (equal). **Peixu Guo:** Conceptualization (equal); Funding acquisition (equal); Methodology (equal); Resources (equal); Software (equal); Supervision (equal); Writing – review & editing (equal). **Chih-Yung Wen:** Conceptualization (equal); Funding acquisition (lead); Methodology (equal); Resources (lead); Software (equal); Supervision (lead); Writing – review & editing (equal).

DATA AVAILABILITY

The data that support the findings of this study are available from the corresponding author upon reasonable request.

APPENDIX A: GRID INDEPENDENCE VERIFICATION FOR TWO-DIMENSIONAL DNS

The grid independence verification for two-dimensional DNS is conducted, and two mesh configurations are considered here: $N_x \times N_y = 3612 \times 220$ and $N_x \times N_y = 4200 \times 320$. Figure 19 presents the distributions of the skin friction coefficient and surface pressure coefficient under two different mesh configurations. In both figures, the short blue and red dashed lines represent the separation and reattachment points, respectively. As can be observed from Fig. 19(a), the scales of the separation bubble obtained by these two mesh configurations are nearly identical, indicating that this mesh configuration $N_x \times N_y = 3612 \times 220$ is sufficient to capture the two-dimensional flow characteristics. Figure 19(b) illustrates how the surface pressure begins to increase upstream of the separation point, as demonstrated by the free-interaction process,[89] before reaching a plateau region. The pressure then re-elevates near the reattachment point, reaching its peak values, as determined by the oblique shock theory. In summary, the mesh resolution $N_x \times N_y = 3612 \times 220$ is sufficient to capture the flow features of the current hypersonic compression flow.

APPENDIX B: GRID INDEPENDENCE VERIFICATION FOR GLOBAL STABILITY ANALYSIS

Figure 20 shows the contour of eigenvalue spectra under two different mesh configurations at $\lambda_z = 19.04$ mm. The red and blue circles represent $N_x \times N_y = 1225 \times 240$ and $N_x \times N_y = 1750 \times 340$, respectively. The no more than 1.0% difference in terms of the maximum growth rates between these two mesh configurations indicates

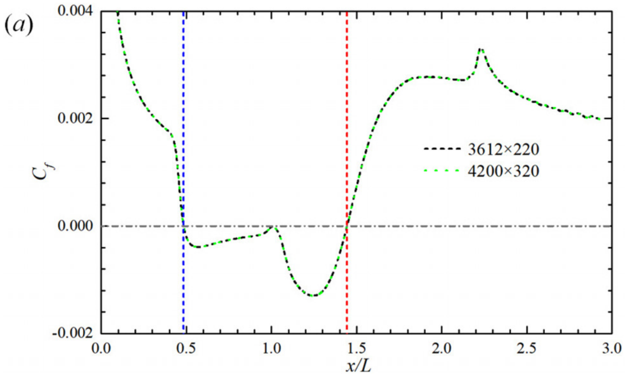

FIG. 19. Distributions of (a) skin friction coefficient and (b) surface pressure coefficient under two different mesh configurations. Short black dashed lines: Nodes number along the streamwise direction $N_x = 3612$, nodes number along the normal direction $N_y = 220$. Green doted lines: $N_x \times N_y = 4200 \times 320$. The short blue and red dashed lines represent the separation and reattachment points, respectively.

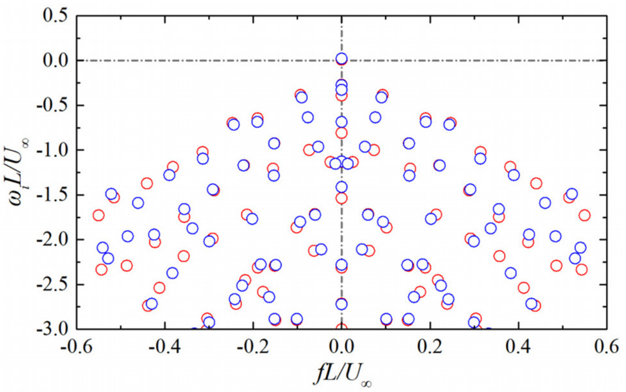

FIG. 20. Contours of eigenvalue spectra under two different mesh configurations at $\lambda_z = 19.04$ mm. Red circles: $N_x \times N_y = 1225 \times 240$; Blue circles: $N_x \times N_y = 1750 \times 340$.

that grid independence is achieved when the number of grids reaches $N_x \times N_y = 1225 \times 240$.

APPENDIX C: LINEAR STABILITY ANALYSIS

The current linear stability analysis considers the issue of convective instabilities caused by small amplitude disturbances within a compressible boundary layer and has been validated by calculating a series of benchmark cases.[90–93] The disturbance manifests in the form of:

$$\boldsymbol{\phi}'(x, y, z, t) = \boldsymbol{\varphi}(y) e^{\mathrm{i}(\alpha x + \beta z - \omega t)} + c.c, \tag{C1}$$

where $\boldsymbol{\varphi} = (\hat{\rho}, \hat{u}, \hat{v}, \hat{w}, \hat{T})^{\mathrm{T}}$ denotes the eigenfunction, β and ω represent the spanwise wavenumber and the angular frequency, respectively. The *c.c* symbol represents the complex conjugate.

$$\alpha = \alpha_r + \mathrm{i}\alpha_i, \tag{C2}$$

where α_r is the streamwise wavenumber, $-\alpha_i$ is the spatial growth rate.

The linearized Navier-Stokes equations are transformed into an eigenvalue problem through the introduction of the parallel-flow assumption, and subsequently solved by a Chebyshev pseudo-spectral method to obtain the global eigenvalue spectrum. During such solving procedures, an iterative compact fourth-order difference scheme is employed to improve the accuracy of the eigenvalue and eigenfunction.[94]

REFERENCES

[1] H. Babinsky and J. K. Harvey, *Shock Wave-Boundary-Layer Interactions* (Cambridge University Press, 2011), Vol. 32.
[2] D. S. Dolling, "Fifty years of shock-wave/boundary-layer interaction research: What next?," AIAA J. **39**, 1517–1531 (2001).
[3] N. T. Clemens and V. Narayanaswamy, "Low-frequency unsteadiness of shock wave/turbulent boundary layer interactions," Annu. Rev. Fluid Mech. **46**, 469–492 (2014).
[4] D. V. Gaitonde, "Progress in shock wave/boundary layer interactions," Prog. Aerosp. Sci. **72**, 80–99 (2015).
[5] S. L. Gai and A. Khraibut, "Hypersonic compression corner flow with large separated regions," J. Fluid Mech. **877**, 471–494 (2019).
[6] A. Sansica, N. D. Sandham, and Z. Hu, "Instability and low-frequency unsteadiness in a shock-induced laminar separation bubble," J. Fluid Mech. **798**, 5–26 (2016).
[7] F. Guiho, F. Alizard, and J.-C. Robinet, "Instabilities in oblique shock wave/laminar boundary-layer interactions," J. Fluid Mech. **789**, 1–35 (2016).
[8] I. Egorov, V. Neiland, and V. Shredchenko, "Three-dimensional flow structures at supersonic flow over the compression ramp," in *49th AIAA Aerospace Sciences Meeting Including the New Horizons Forum and Aerospace Exposition* (AIAA, 2011), p. 730.
[9] J. M. Kendall, "Wind tunnel experiments relating to supersonic and hypersonic boundary-layer transition," AIAA J. **13**, 290–299 (1975).
[10] X. Zhong and X. Wang, "Direct numerical simulation on the receptivity, instability, and transition of hypersonic boundary layers," Annu. Rev. Fluid Mech. **44**, 527–561 (2012).
[11] E. Reshotko, "Transition issues for atmospheric entry," J. Spacecr. Rockets **45**, 161–164 (2008).
[12] L. Fu, M. Karp, S. T. Bose, P. Moin, and J. Urzay, "Shock-induced heating and transition to turbulence in a hypersonic boundary layer," J. Fluid Mech. **909**, A8 (2021).
[13] S. Cao, J. Hao, I. Klioutchnikov, C.-Y. Wen, H. Olivier, and K. A. Heufer, "Transition to turbulence in hypersonic flow over a compression ramp due to intrinsic instability," J. Fluid Mech. **941**, A8 (2022).

[14] M. Lugrin, S. Beneddine, C. Leclercq, E. Garnier, and R. Bur, "Transition scenario in hypersonic axisymmetrical compression ramp flow," J. Fluid Mech. **907**, A6 (2021).

[15] A. Novikov, I. Egorov, and A. Fedorov, "Direct numerical simulation of wave packets in hypersonic compression-corner flow," AIAA J. **54**, 2034–2050 (2016).

[16] J. Hao, S. Cao, P. Guo, and C.-Y. Wen, "Response of hypersonic compression corner flow to upstream disturbances," J. Fluid Mech. **964**, A25 (2023).

[17] T. Herbert, "Secondary instability of boundary layers," Annu. Rev. Fluid Mech. **20**, 487–526 (1988).

[18] L. M. Mack, "Review of linear compressible stability theory," in *Stability of Time Dependent and Spatially Varying Flows: Proceedings of the Symposium on the Stability of Time Dependent and Spatially Varying Flows Held August 19–23, 1985, at NASA Langley Research Center, Hampton, Virginia* (Springer, 1987) pp. 164–187.

[19] W. S. Saric, H. L. Reed, and E. B. White, "Stability and transition of three-dimensional boundary layers," Annu. Rev. Fluid Mech. **35**, 413–440 (2003).

[20] S. A. Craig and W. S. Saric, "Crossflow instability in a hypersonic boundary layer," J. Fluid Mech. **808**, 224–244 (2016).

[21] A. Fedorov, "Transition and stability of high-speed boundary layers," Annu. Rev. Fluid Mech. **43**, 79–95 (2011).

[22] W. S. Saric, "Görtler vortices," Annu. Rev. Fluid Mech. **26**, 379–409 (1994).

[23] Y. S. Kachanov, "Physical mechanisms of laminar-boundary-layer transition," Annu. Rev. Fluid Mech. **26**, 411–482 (1994).

[24] C. Lee and J. Wu, "Transition in wall-bounded flows," Appl. Mech. Rev. **61**, 030802 (2008).

[25] L. M. Mack, "Linear stability theory and the problem of supersonic boundary-layer transition," AIAA J. **13**, 278–289 (1975).

[26] L. M. Mack, "Boundary-layer linear stability theory," AGARD Report No. 709, 1984.

[27] L. M. Mack, *Boundary-Layer Stability Theory* (Jet Propulsion Laboratory, 1969).

[28] P. Balakumar, H. Zhao, and H. Atkins, "Stability of hypersonic boundary layers over a compression corner," AIAA J. **43**, 760–767 (2005).

[29] C. S. Butler and S. J. Laurence, "Interaction of second-mode disturbances with an incipiently separated compression-corner flow," J. Fluid Mech. **913**, R4 (2021).

[30] C. S. Butler and S. J. Laurence, "Transitional hypersonic flow over slender cone/flare geometries," J. Fluid Mech. **949**, A37 (2022).

[31] K. M. Casper, S. J. Beresh, and S. P. Schneider, "Pressure fluctuations beneath instability wavepackets and turbulent spots in a hypersonic boundary layer," J. Fluid Mech. **756**, 1058–1091 (2014).

[32] S. Laurence, A. Wagner, and K. Hannemann, "Experimental study of second-mode instability growth and breakdown in a hypersonic boundary layer using high-speed schlieren visualization," J. Fluid Mech. **797**, 471–503 (2016).

[33] K. J. Franko and S. K. Lele, "Breakdown mechanisms and heat transfer overshoot in hypersonic zero pressure gradient boundary layers," J. Fluid Mech. **730**, 491–532 (2013).

[34] J. Sivasubramanian and H. F. Fasel, "Numerical investigation of the development of three-dimensional wavepackets in a sharp cone boundary layer at Mach 6," J. Fluid Mech. **756**, 600–649 (2014).

[35] J. Sivasubramanian and H. F. Fasel, "Direct numerical simulation of transition in a sharp cone boundary layer at Mach 6: Fundamental breakdown," J. Fluid Mech. **768**, 175–218 (2015).

[36] E. K. Benitez, M. P. Borg, P. Paredes, S. P. Schneider, and J. S. Jewell, "Measurements of an axisymmetric hypersonic shear-layer instability on a cone-cylinder-flare in quiet flow," Phys. Rev. Fluids **8**, 083903 (2023).

[37] P. Paredes, A. Scholten, M. M. Choudhari, F. Li, E. K. Benitez, and J. S. Jewell, "Boundary-layer instabilities over a cone–cylinder–flare model at Mach 6," AIAA J. **60**, 5652–5661 (2022).

[38] E. K. Benitez, M. P. Borg, A. Scholten, P. Paredes, Z. McDaniel, and J. S. Jewell, "Instability and transition onset downstream of a laminar separation bubble at Mach 6," J. Fluid Mech. **969**, A11 (2023b).

[39] D. Xu, J. Liu, and X. Wu, "Görtler vortices and streaks in boundary layer subject to pressure gradient: Excitation by free stream vortical disturbances, nonlinear evolution and secondary instability," J. Fluid Mech. **900**, A15 (2020).

[40] S. Cao, J. Hao, P. Guo, C.-Y. Wen, and I. Klioutchnikov, "Stability of hypersonic flow over a curved compression ramp," J. Fluid Mech. **957**, A8 (2023).

[41] D. Xu, P. Ricco, and L. Duan, "Görtler instability and transition in compressible flows," AIAA J. **62**, 489–517 (2024).

[42] G. Huang, W. Si, and C. Lee, "Early stage evolution of naturally developing Görtler streaks," Phys. Fluids **33**, 061706 (2021).

[43] G. Huang, "Interactions between Görtler vortices and the second mode in hypersonic boundary layer," Phys. Fluids **33**, 111701 (2021).

[44] G. Huang, W. Si, and C. Lee, "Inner structures of Görtler streaks," Phys. Fluids **33**, 034116 (2021).

[45] X. Li, Y. Zhang, H. Yu, Z.-K. Lin, H.-J. Tan, and S. Sun, "Görtler vortices behavior and prediction in dual-incident shock-wave/turbulent-boundary-layer interactions," Phys. Fluids **34**, 106103 (2022).

[46] X. Chen, G. Huang, and C. Lee, "Hypersonic boundary layer transition on a concave wall: Stationary Görtler vortices," J. Fluid Mech. **865**, 1–40 (2019).

[47] X. Chen, J. Chen, X. Yuan, G. Tu, and Y. Zhang, "From primary instabilities to secondary instabilities in Görtler vortex flows," Adv. Aerodyn. **1**, 19 (2019).

[48] G. Huang, X. Chen, J. Chen, X. Yuan, and G. Tu, "The stabilizing effect of grooves on Görtler instability-induced boundary layer transition in hypersonic flow," Phys. Fluids **35**, 041701 (2023).

[49] X. Chen, J. Chen, and X. Yuan, "Hypersonic boundary layer transition on a concave wall induced by low-frequency blowing and suction," Phys. Fluids **34**, 114105 (2022).

[50] P. Chuvakhov and V. Radchenko, "Effect of Görtler-like vortices of various intensity on heat transfer in supersonic compression corner flows," Int. J. Heat Mass Transfer **150**, 119310 (2020).

[51] S. Cao, J. Hao, I. Klioutchnikov, H. Olivier, K. A. Heufer, and C.-Y. Wen, "Leading-edge bluntness effects on hypersonic three-dimensional flows over a compression ramp," J. Fluid Mech. **923**, A27 (2021).

[52] S. Cao, J. Hao, I. Klioutchnikov, H. Olivier, and C.-Y. Wen, "Unsteady effects in a hypersonic compression ramp flow with laminar separation," J. Fluid Mech. **912**, A3 (2021).

[53] S. Cao, I. Klioutchnikov, and H. Olivier, "Görtler vortices in hypersonic flow on compression ramps," AIAA J. **57**, 3874–3884 (2019).

[54] S. Gottlieb and C.-W. Shu, "Total variation diminishing Runge-Kutta schemes," Math. Comput. **67**, 73–85 (1998).

[55] G.-S. Jiang and C.-W. Shu, "Efficient implementation of weighted ENO schemes," J. Comput. Phys. **126**, 202–228 (1996).

[56] V. Hermes, I. Klioutchnikov, and H. Olivier, "Linear stability of WENO schemes coupled with explicit Runge–Kutta schemes," Int. J. Numer. Methods Fluids **69**, 1065–1095 (2012).

[57] S. Cao, H. Olivier, and W. Schröder, "Streamwise vortices in hypersonic flow on a compression ramp," Ph.D. thesis (RWTH Aachen University, 2021).

[58] J. Hao, S. Cao, C.-Y. Wen, and H. Olivier, "Occurrence of global instability in hypersonic compression corner flow," J. Fluid Mech. **919**, A4 (2021).

[59] D. Sorensen, R. Lehoucq, C. Yang, and K. Maschhoff, "ARPACK software, version 2.3," (1996).

[60] D. Sipp and O. Marquet, "Characterization of noise amplifiers with global singular modes: The case of the leading-edge flat-plate boundary layer," Theor. Comput. Fluid Dyn. **27**, 617–635 (2013).

[61] B. Bugeat, J.-C. Chassaing, J.-C. Robinet, and P. Sagaut, "3D global optimal forcing and response of the supersonic boundary layer," J. Comput. Phys. **398**, 108888 (2019).

[62] A. Dwivedi, G. Sidharth, J. W. Nichols, G. V. Candler, and M. R. Jovanović, "Reattachment streaks in hypersonic compression ramp flow: An input–output analysis," J. Fluid Mech. **880**, 113–135 (2019).

[63] G. S. Sidharth, A. Dwivedi, G. V. Candler, and J. W. Nichols, "Onset of three-dimensionality in supersonic flow over a slender double wedge," Phys. Rev. Fluids **3**, 093901 (2018).

[64] J.-P. Boin, J. C. Robinet, C. Corre, and H. Deniau, "3D steady and unsteady bifurcations in a shock-wave/laminar boundary layer interaction: A numerical study," Theor. Comput. Fluid Dyn. **20**, 163–180 (2006).

[65] J.-C. Robinet, "Bifurcations in shock-wave/laminar-boundary-layer interaction: Global instability approach," J. Fluid Mech. **579**, 85–112 (2007).

[66] N. Hildebrand, A. Dwivedi, J. W. Nichols, M. R. Jovanović, and G. V. Candler, "Simulation and stability analysis of oblique shock-wave/boundary-layer interactions at Mach 5.92," Phys. Rev. Fluids **3**, 013906 (2018).

[67] V. Theofilis, S. Hein, and U. Dallmann, "On the origins of unsteadiness and three-dimensionality in a laminar separation bubble," Philos. Trans. R Soc. London, Ser. A **358**, 3229–3246 (2000).

[68] B. Bugeat, J.-C. Robinet, J.-C. Chassaing, and P. Sagaut, "Low-frequency resolvent analysis of the laminar oblique shock wave/boundary layer interaction," J. Fluid Mech. **942**, A43 (2022).

[69] M. Landahl, "A note on an algebraic instability of inviscid parallel shear flows," J. Fluid Mech. **98**, 243–251 (1980).

[70] P. Hall, "The linear development of Görtler vortices in growing boundary layers," J. Fluid Mech. **130**, 41–58 (1983).

[71] A. Bottaro and P. Luchini, "Görtler vortices: Are they amenable to local eigenvalue analysis?," Eur. J. Mech.-B/Fluids **18**, 47–65 (1999).

[72] J. Ren and S. Fu, "Secondary instabilities of Görtler vortices in high-speed boundary layer flows," J. Fluid Mech. **781**, 388–421 (2015).

[73] C. Hader and H. F. Fasel, "Towards simulating natural transition in hypersonic boundary layers via random inflow disturbances," J. Fluid Mech. **847**, R3 (2018).

[74] P. Welch, "The use of fast Fourier transform for the estimation of power spectra: A method based on time averaging over short, modified periodograms," IEEE Trans. Audio Electroacoust. **15**, 70–73 (1967).

[75] L. Duan, I. Beekman, and M. Martin, "Direct numerical simulation of hypersonic turbulent boundary layers. Part 2. Effect of wall temperature," J. Fluid Mech. **655**, 419–445 (2010).

[76] A. Walz, *Boundary Layers of Flow and Temperature* (The Massachusetts Institute of Technology Press, Cambridge, MA, 1969), p. 297.

[77] L. Duan and M. Martin, "Direct numerical simulation of hypersonic turbulent boundary layers. Part 4. Effect of high enthalpy," J. Fluid Mech. **684**, 25–59 (2011).

[78] C. Lee and X. Jiang, "Flow structures in transitional and turbulent boundary layers," Phys. Fluids **31**, 111301 (2019).

[79] F. Li and M. R. Malik, "Fundamental and subharmonic secondary instabilities of Görtler vortices," J. Fluid Mech. **297**, 77–100 (1995).

[80] P. Hall and N. J. Horseman, "The linear inviscid secondary instability of longitudinal vortex structures in boundary layers," J. Fluid Mech. **232**, 357–375 (1991).

[81] K. Gray, "Instability and transition on slender cones under fully quiet Mach-6 flow," Ph.D. thesis (Purdue University, 2022).

[82] E. K. Benitez, M. P. Borg, and J. L. Hill, "Nosetip bluntness effects on a cone-cylinder-flare at Mach 6," Exp. Fluids **65**, 72 (2024).

[83] X. Chen, Y. Zhu, and C. Lee, "Interactions between second mode and low-frequency waves in a hypersonic boundary layer," J. Fluid Mech. **820**, 693–735 (2017).

[84] R. Song, L. Zhao, and Z. Huang, "Secondary instability of stationary Görtler vortices originating from first/second Mack mode," Phys. Fluids **32**, 034109 (2020).

[85] J. D. Swearingen and R. F. Blackwelder, "The growth and breakdown of streamwise vortices in the presence of a wall," J. Fluid Mech. **182**, 255–290 (1987).

[86] J. Hofferth, R. Humble, D. Floryan, and W. Saric, "High-bandwidth optical measurements of the second-mode instability in a Mach 6 quiet tunnel," in *51st AIAA Aerospace Sciences Meeting Including the New Horizons Forum and Aerospace Exposition* (AIAA, 2013), p. 378.

[87] J. Ren, S. Fu, and A. Hanifi, "Stabilization of the hypersonic boundary layer by finite-amplitude streaks," Phys. Fluids **28**, 024110 (2016).

[88] H. Bippes, "Basic experiments on transition in three-dimensional boundary layers dominated by crossflow instability," Prog. Aerosp. Sci. **35**, 363–412 (1999).

[89] D. R. Chapman, D. M. Kuehn, and H. K. Larson, "Investigation of separated flows in supersonic and subsonic streams with emphasis on the effect of transition," NACA-TR-1356, January 1958.

[90] P. Guo, Z. Gao, C. Jiang, and C.-H. Lee, "Linear stability analysis on the most unstable frequencies of supersonic flat-plate boundary layers," Comput. Fluids **197**, 104394 (2020).

[91] P. Guo, Z. Gao, C. Jiang, and C.-H. Lee, "Sensitivity analysis on supersonic-boundary-layer stability subject to perturbation of flow parameters," Phys. Fluids **33**, 084111 (2021).

[92] P. Guo, F. Shi, Z. Gao, C. Jiang, C.-H. Lee, and C. Wen, "Sensitivity analysis on supersonic-boundary-layer stability: Parametric influence, optimization, and inverse design," Phys. Fluids **34**, 104113 (2022).

[93] P. Guo, F. Shi, Z. Gao, C. Jiang, C.-H. Lee, and C. Wen, "Heat transfer and behavior of the Reynolds stress in Mach 6 boundary layer transition induced by first-mode oblique waves," Phys. Fluids **34**, 104116 (2022).

[94] M. R. Malik, "Numerical methods for hypersonic boundary layer stability," J. Comput. Phys. **86**, 376–413 (1990).